Corrosion Science 252 (2025) 112961

Contents lists available at ScienceDirect

Corrosion Science

journal homepage: www.elsevier.com/locate/corsci

Localized corrosion in anodized aluminium alloys: The role of constituent particle-induced defects in anodic films

João Victor de S. Araujo [a,*], Jinghui Chen [b], Isolda Costa [a], Xiaorong Zhou [b]

[a] Centro de Ciência e Tecnologia de Materiais, Instituto de Pesquisas Energéticas e Nucleares, IPEN/CNEN, Av. Prof. Prof. Lineu Prestes, São Paulo 2242, Brazil
[b] Corrosion and Protection Centre, School of Materials, The University of Manchester, Manchester M13 9PL, UK

ARTICLE INFO

Keywords:
High-strength aluminium alloys
Anodizing
Particle-induced defects
Corrosion resistance

ABSTRACT

The influence of defects formed by dissolution of constituent intermetallic particles (IMPs) on the corrosion resistance of anodized aluminium alloys, including AA2024-T3, AA2198-T8, AA2198-T851, and AA7475-T761, is investigated. Localized corrosion initiates cavity defects located at the film/alloy interface, mainly due to the dissolution of high-copper-containing IMPs. In AA2024, Si-containing particle-induced defects also contributed to a reduction in corrosion resistance. Low-copper-containing IMPs in AA7475-T761 alloy, however, do not affect corrosion resistance. The effects of particle density, composition, size, and location on the formation of defects in anodic films and, subsequently, on corrosion resistance of anodized alloys are discussed.

1. Introduction

The anodic film typically developed on pure aluminium is well-known for its continuous and uniform characteristics, providing an effective barrier against corrosion [1,2]. However, the microstructural heterogeneity of commercial aluminium alloys may adversely affect the quality of the anodic film [3,4]. The final properties of anodic films are influenced by nanometric strengthening precipitates (formed during ageing) and micrometric constituent intermetallic particles (IMPs) (originating from the casting process) in the alloys [5]. While nanometric precipitates primarily affect the optical properties of the anodic films [6,7], IMPs play a critical role in determining their corrosion resistance [8]. IMPs, which often contain elements such as copper, iron, manganese, and silicon, are prone to dissolution during anodizing process, resulting in micrometric cavities that compromise the integrity of the anodic film [9]. Such issues are particularly significant in aluminium alloys used in the aerospace industry, where anodizing is crucial for achieving the necessary corrosion resistance under demanding operational conditions [8].

While many studies suggest that defects in the anodic film reduce corrosion resistance, most rely on electrochemical data, such as polarization curves and Electrochemical Impedance Spectroscopy (EIS) [10–25], without providing details about the corrosion processes at defects or corrosion sites. According to the literature, corrosion tends to initiate at defects resulting from the dissolution of IMPs during the anodizing process [26], which may appear as surface discontinuities, weak points at the film/alloy interface, or internal voids that compromise the overall integrity of the anodic film. Although it is well established that corrosion occurs only when the underlying metal is exposed to the corrosive environment, the precise location where this process initiates remains a topic of debate. Some studies associate the reduction in corrosion resistance with defects on the anodic film surface [11,13,27,28]; others attribute it to imperfections within the film or at the film/alloy interface [29], leading to conflicting interpretations. Additionally, while some investigations suggest that corrosion initiates at defects within the anodic film [30–33], others argue that it primarily occurs at sites where the film is disrupted, allowing localized exposure of the substrate [11–13,16,28,34,35]. Another hypothesis posits that the corrosion process originates at the film/alloy interface [29,36,37].

Despite these findings, many studies fail to directly correlate the presence of IMP-related defects with the corrosion resistance of anodized alloys. Although some researchers have examined the anodizing behaviour of IMPs, their analyses often lack a comprehensive assessment of how these defects specifically influence the corrosion mechanisms of anodized alloys [30,38–96]. Furthermore, other studies have overlooked corrosion resistance, concentrating solely on the mechanical performance of anodized alloys [97–102]. Nonetheless, such works indicate that the dissolution of IMPs can lead to the formation of micrometric cavities in the anodic film, thereby significantly compromising its integrity. While this issue is acknowledged, some of these

* Corresponding author.
E-mail address: jvaraujo@alumni.usp.br (J.V.S. Araujo).

https://doi.org/10.1016/j.corsci.2025.112961
Received 28 February 2025; Received in revised form 13 April 2025; Accepted 18 April 2025
Available online 21 April 2025

studies have not employed appropriate methodologies to thoroughly assess the impact of these particles on corrosion behaviour, highlighting a significant gap in the existing literature.

In contrast, a few studies [33,36], particularly those focused on AA2099 Al-Cu-Li alloys, have demonstrated that defects arising from IMP dissolution are primarily responsible for the reduction in corrosion resistance. However, these investigations were limited, providing only surface-level images of the corroded alloys after film removal and lacking detailed cross-sectional analysis [33]. Another study [36] suggested that defects at the film/alloy interface were the main contributors to the loss of corrosion resistance. However, this research primarily addressed the anodizing behaviour of intermetallic particles rather than systematically evaluating their role in corrosion resistance.

More recently, a study [29] proposed a schematic diagram illustrating the development of corrosion in anodized aluminium alloys, emphasizing the role of micrometric defects. However, this work was restricted to AA2055 alloy, raising the question of whether this mechanism applies to other aluminium alloys. Moreover, recent publications present conflicting findings: some suggest that corrosion predominantly initiates at surface defects [34], while others highlight internal defects as the primary sites of corrosive attack [103]. Additional research has investigated how variations in anodizing parameters and post-treatments influence corrosion resistance [104–109]. While these studies acknowledge that defects in the anodic film compromise corrosion resistance, they do not clearly establish which types of defects are most critical for the initiation and progression of localized corrosion in anodized alloys.

This study seeks to address these gaps by investigating the influence of defects originating from IMPs during anodizing of various aluminium alloys on their corrosion behaviour, thereby advancing the understanding of localized corrosion mechanisms. IMPs, whose quantity and size are often determined by manufacturing processes, pose a persistent challenge. Therefore, this work emphasizes the need for strategies to mitigate the adverse effects of these defects on anodized alloy performance. By providing a detailed characterization of the corrosion behaviour of these alloys, this study aims to develop targeted approaches to enhance corrosion resistance and improve durability in aggressive environments.

The central scientific question guiding this research is: How do micrometric defects, generated by constituent intermetallic particles, influence the initiation and progression of localized corrosion in different anodized aluminium alloys?

2. Experimental

This study focuses on the commercial aluminium alloys AA2024-T3 (Al–Cu–Mg), AA2198-T8 and AA2198-T851 (Al–Cu–Li), and AA7475-T761 (Al–Zn–Mg), provided in the form of rolled sheets. The compositions of these alloys, determined by ICP-OES, are presented in Table 1. The alloys were analyzed in their respective commercial temper conditions: T3 for AA2024 (solution heat-treated, cold-worked, and naturally aged); T8 and T851 for AA2198 (solution heat-treated, cold-worked, and artificially aged, with T851 involving additional stretching); and T761 for AA7475 (solution heat-treated, cold-worked, stress-relieved, and artificially aged).

These four alloys were selected to provide a representative overview of different families of high-strength aluminium alloys used in aerospace applications [8]. AA2024-T3 alloy is widely used and extensively studied, especially regarding its corrosion behaviour after anodizing. AA2198-T8 and AA2198-T851 alloys, as part of the newer Al–Cu–Li alloy family, are promising alternatives to AA2024, offering improved mechanical performance and reduced density, but remain less explored in terms of anodized corrosion behaviour. The AA7475-T761 alloy represents the 7XXX series, which is well known in the literature, though this specific alloy is comparatively underexplored, particularly in comparison to AA7075 alloy. All these observations are in line with the recent comprehensive review on the effect of microstructure on the corrosion behaviour of anodized aluminium alloys [9], which guided the selection and contextualisation of the alloys examined in this study.

Table 1
Chemical composition of the studied alloys (wt%) obtained by inductively coupled plasma optical emission spectrometry (ICP-OES).

Elements	Aluminium alloys			
	AA2024-T3	AA2198-T8	AA2198-T851	AA7475-T761
Al	Balance			
Cu	4.8 (3.8–4.9)	3.34 (2.9–3.5)	3.31 (2.9–3.5)	1.52 (1.2–1.9)
Mg	0.59 (1.2–1.8)	0.31 (0.25–0.80)	0.31 (0.25–0.80)	1.8 (1.9–2.6)
Mn	0.52 (0.3–0.9)	0.003 (≤ 0.50)	0.003 (≤ 0.50)	0.05 (≤ 0.06)
Li	–	0.95 (0.81–1.1)	0.96 (0.81–1.1)	–
Fe	0.18 (≤ 0.5)	0.04 (≤ 0.10)	0.04 (≤ 0.10)	0.07 (≤ 0.12)
Zn	0.11 (≤ 0.25)	0.006 (≤ 0.35)	0.006 (≤ 0.35)	6.10 (5.2–6.2)
Si	0.07 (≤ 0.5)	0.04 (≤ 0.08)	0.03 (≤ 0.08)	0.03 (≤ 0.06)
Zr	–	0.05 (0.04–0.18)	0.05 (0.04–0.18)	–
Ag	–	0.26 (0.2–0.3)	0.25 (0.2–0.3)	–
Cr	–	–		0.20 (0.18 – 0.25)

Note: Values in parentheses present the composition specification according to ASM [110] for aluminium alloys.

The alloy surfaces were mechanically ground using silicon carbide sandpaper with progressively finer grit sizes (P800, P1200, P2400, and P4000), followed by sequential polishing with 3 μm and 1 μm diamond pastes. After mechanical polishing, the specimens were degreased in acetone, rinsed with deionized water, and dried with a cold air jet. After polishing, the samples were anodized without undergoing any chemical or electrochemical pretreatment. This approach was intentionally adopted to investigate the behaviour of constituent intermetallic particles during anodizing, the formation of defects, and their correlation with the initiation of corrosion observed after immersion testing.

Anodizing was conducted in a tartaric-sulfuric acid (TSA) solution [111] composed of 0.46 mol L^{-1} sulfuric acid and 0.53 mol L^{-1} tartaric acid, maintained at 37 ± 1 °C. Circular specimens were used for anodizing due to the geometry of the electrochemical cell. The exposed surface area of the samples was 1 cm^2, with a platinum mesh (6 cm × 10 cm) serving as the counter electrode. The anodizing process was conducted at a constant voltage of 14 V for 20 min, with continuous current density monitoring using a KR50003–500 V / 3 DC power supply.

After anodization, the specimens were immersed in a 0.1 mol L^{-1} NaCl aqueous solution at room temperature (approximately 20 °C) for 12, 24, 48, and 60 h. Immersion tests were performed in triplicate for each exposure condition, using an exposed surface area of 1 cm^2. Cross-sectional analysis of the anodic films was performed by embedding the samples in phenolic resin, preparing them as a sandwich, and cutting them along their central axis. The specimens were metallographically prepared by mechanical grinding and polishing with diamond paste. Cross-sections of the anodized specimens post-corrosion testing were also prepared using ultramicrotomy (Leica Ultracut) with a diamond knife, enabling high-precision cuts for detailed analysis. Corrosion sites were selected based on surface inspection and marked for sectioning. The selected areas were trimmed using a glass knife, with slicing speed set to 3 mm/s and slicing thickness to 3 μm. Subsequently, the pit region was cross sectioned with a diamond knife at a slicing speed of 1 mm/s and slicing thickness of 500 nm or 1 μm.

Surface characterization, both before and after anodization, as well as after the immersion test, was performed using optical microscopy (OM) and scanning electron microscopy (SEM). Optical microscopy was carried out with a ZEISS Axiovert 5 digital microscope in bright field

mode, while SEM analysis was conducted using a Quanta 650 microscope operating at 20 kV, equipped with an energy-dispersive X-ray spectroscopy (EDX) system. High-resolution imaging was obtained with a Zeiss Ultra 55 microscope operating at 1.5 kV to minimize charging effects. Statistical analysis of corrosion site dimensions was performed using ImageJ® software [112].

To expose corrosion beneath the anodic film after immersion testing, the anodic film was stripped by immersing the tested samples in a desmutting solution containing 20 g of CrO_3 and 30 mL of H_3PO_4 per liter of deionized water at 60 °C for 3 min. Following the removal of the anodic film and corrosion products, the samples were immersed in distilled water in an ultrasonic bath for 20 min and then dried with a cool air stream.

3. Results

3.1. Anodizing behaviour of constituent intermetallic particles (IMPs): surface and cross-sectional analysis with focus on defect formation

To assess the behaviour of IMPs during anodizing, the surface of the aluminium alloys was examined before and after the process, as shown in Fig. 1.

Fig. 1 displays SEM images of the aluminium alloys in the as-polished condition (a–d) and after anodizing (e–h), both acquired at low magnification. The images in (a1–d1) and (e1–h1) correspond to higher magnification views of the regions marked by dashed squares, emphasizing areas containing IMPs. The red and blue dots in these images indicate the spots selected for EDX analysis, with the results summarized in Table 2.

In the AA2024-T3 alloy (Fig. 1 (a1)), three types of IMPs were analysed: Al–Cu–Mg (S1 in Table 2), Al–Cu–Fe–Mn (S2 in Table 2), and Al–Cu–Fe–Mn–Si (S3 in Table 2). In the AA2198-T8 (Fig. 1 (b1)) and AA2198-T851 (Fig. 1 (c1)) alloys, a single type of IMP was analysed, composed of Al–Cu–Fe (S9 and S13 in Table 2). For the AA7475-T761 alloy (Fig. 1 (d1)), two types of IMPs were identified: Al–Cu–Fe with high-copper-content (S17 in Table 2) and Al–Cu–Fe with low-copper-content (S18 in Table 2). The classification of these intermetallic particles into high- and low-copper-content categories is based on previous studies in the literature [113,114], which consider IMPs with copper content > 12 wt% as high-copper-content and those with < 7 wt% as low-copper-content. Additionally, the literature classifies IMPs with copper content between 7 wt% and 12 wt% as medium-copper-content [114].

The substantial increase in oxygen and sulfur contents after anodizing (compare corresponding points S4, S10, S14, and S19 with S8, S12, S16, and S22 in Table 2) is due to the anodic film formed. The analysis of regions containing IMPs after anodizing (Fig. 1 (e1–h1)) revealed the formation of cavities whose morphology resembles that of the original IMPs, suggesting their dissolution. According to the literature, these cavities are considered defects in the anodic film [30]. EDX analyses in these areas confirmed this hypothesis. In the AA2024-T3, AA2198-T8/T851, and AA7475-T761 alloys, the defects formed by

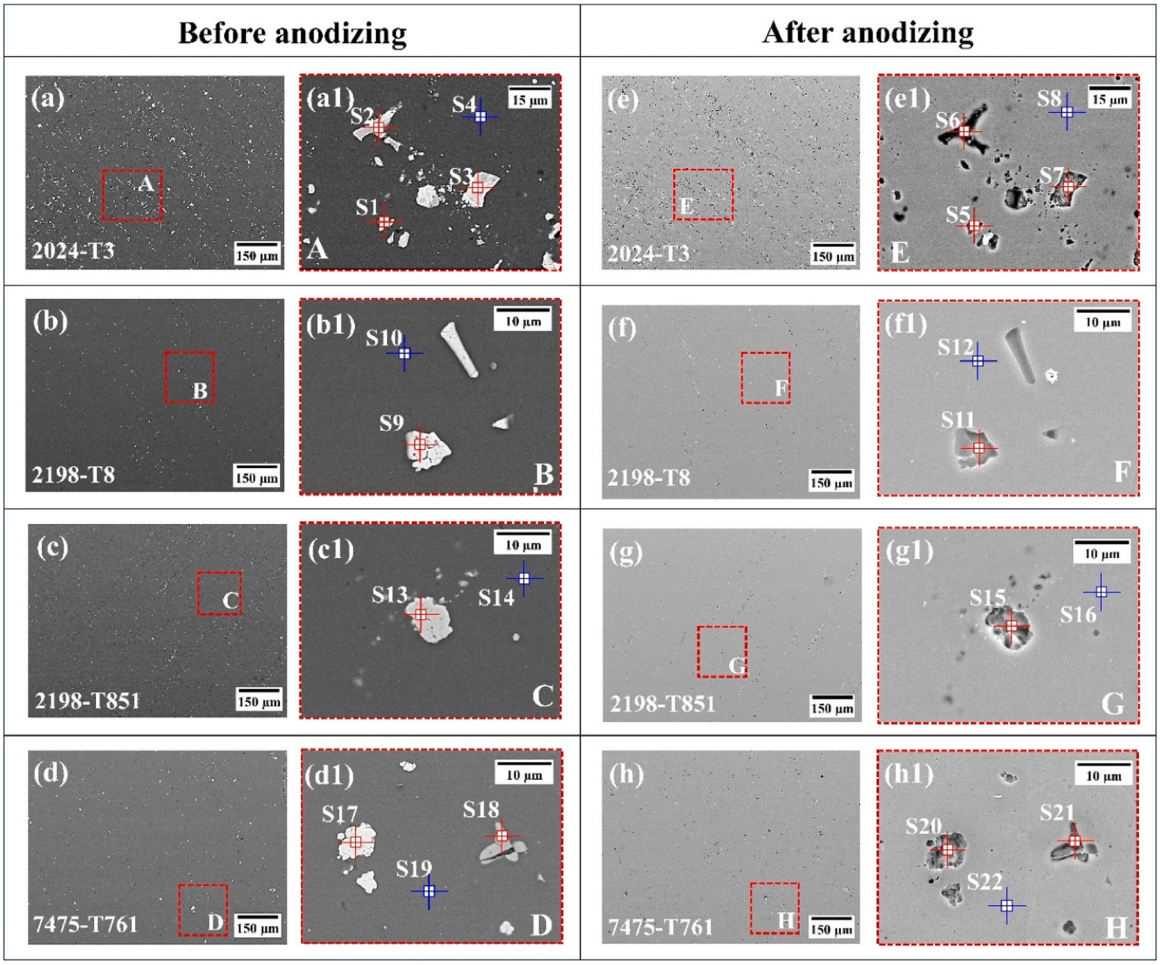

Fig. 1. Scanning electron micrographs of the tested aluminium alloys, before (a–d) and after (e–h) anodizing. (a1–d1) show higher magnification of the dashed square in (a–d); similarly, (e1–h1) show higher magnification of the dashed square in (e–h). Red and blue points in images (a1–d1) and (e1–h1) indicate the locations of EDX analysis (Table 2), before and after anodizing. All images were acquired in backscattered electron (BSE) mode at an accelerating voltage of 20 kV.

Table 2
EDX analysis at locations indicated in Fig. 1 before and after anodizing.

Aluminium Alloys	Test condition of surface	EDX points	Elements (wt%)								
			Al	Cu	Fe	Mg	Mn	O	S	Si	Zn
AA2024-T3	Before anodizing	S1	65.8	26.8	-	10.4	-	-	-	-	-
		S2	78.3	14.2	4.1	-	3.4	-	-	-	-
		S3	75.4	13.2	4.6	-	3.6	-	-	3.2	-
		S4	95.8	3.1	-	1.1	-	-	-	-	-
	After anodizing	S5	69.2	1.1	-	-		28.4	1.3	-	-
		S6	67.2	1.6	-	-	-	30.1	1.1	-	-
		S7	75.6	1.2	-	-	-	21.3	1.1	0.8	-
		S8	67.4	-	-	-	-	31.4	1.2	-	-
AA2198-T8	Before anodizing	S9	59.1	29.1	11.8	-	-	-	-	-	-
		S10	96.3	3.4	-	0.3	-	-	-	-	-
	After anodizing	S11	68.5	1.8	-	-	-	28.5	1.2	-	-
		S12	68.5	-	-	-	-	30.4	1.1	-	-
AA2198-T851	Before anodizing	S13	59.5	30.1	10.4	-	-	-	-	-	-
		S14	96.6	3.1	-	0.3	-	-	-	-	-
	After anodizing	S15	69.5	1.2	-	-	-	28.2	1.1	-	-
		S16	69.3	-	-	-	-	29.6	1.1	-	-
AA7475-T761	Before anodizing	S17	54.5	29.1	16.4	-	-	-	-	-	-
		S18	75.7	5.8	18.5	-	-	-	-	-	-
		S19	89.8	1.3	-	2.8	-	-	-	-	6.1
	After anodizing	S20	70.2	1.1	-	-	-	28.6	1.2	-	-
		S21	75.9	1.9	-	-	-	20.1	1.1	-	-
		S22	67.5	-	-	-	-	30.1	1.1	-	1.3

* Lithium cannot be detected by the EDX employed in the present work.

dissolution of high-copper-containing IMPs showed a significant reduction in Cu, Fe, Mn, and Mg content, alongside a substantial increase in oxygen and sulphur concentrations (S5–S7, S11, S13, and S20 in Table 2). These concentrations were similar to those found in the anodized matrix (S8, S12, S16, and S22 in Table 2), corroborating the complete dissolution of the high-copper-containing IMPs. These findings show that the oxide formed is distributed both within the cavities and throughout the alloy matrix.

In contrast, the cavities resulting from the dissolution of Si-containing particles in the AA2024-T3 alloy, and low-copper-containing particles in the AA7475-T761 alloy, displayed lower oxygen concentrations relative to the surrounding matrix, indicating a slower oxide growth rate in these regions (S7 and S21 in Table 2). In the AA2024-T3 alloy, a slight residual concentration of silicon was also observed after anodizing (S7 in Table 2), which aligns with findings from other studies on the anodizing behaviour of this alloy in sulfuric acid. Silicon has a less negative Gibbs free energy for oxide formation compared to alumina, which hinders co-oxidation with aluminium during anodizing [5]. This explains the residual silicon in the cavities formed by the dissolution of particles containing this element. These results indicate that anodizing behaviour of IMPs varies significantly and cannot be generalized. Small variations in the composition of the IMPs, such as the presence of silicon in the AA2024-T3 alloy, or the reduced copper content in the AA7475-T761 alloy, affect the dissolution rate of the IMPs during anodizing.

Although our study did not focus on short anodizing times to investigate the initial stages of IMP dissolution, previous research indicates that the high-copper-containing IMPs intensifies oxygen generation, leading to the rapid breakdown of the oxide film [115,116]. This results in a fragile film that is easily dissolved in the electrolyte. This phenomenon explains the presence of cavities (Fig. 1 (b1–b4)) in regions with high-copper-containing IMPs after anodizing. The intense oxygen generation at the particle/oxide interface, driven by the oxidation of copper and iron, produces a defective oxide that allows the electrolyte to quickly reach the particle substrate, accelerating its dissolution [117].

In Al-Cu-Li alloys, although lithium was not detected in the IMPs, due to the limitations of EDX, the literature confirms its presence in the particles through advanced characterization techniques [118]. The co-oxidation of lithium forms an oxide that dissolves easily in acidic environments, further accelerating the oxidation rate of high-copper-containing IMPs [117,119].

As shown in Fig. 1, the dissolution of IMPs led to the formation of defects, such as cavities, which significantly affected the surface of the anodic films. The cross-sectional view presented in Fig. 2 provides a more detailed perspective on these defects and their implications for the structural integrity of the anodic films.

Fig. 2(a) shows surface images of the anodic films from the tested alloys. In Fig. 2 (a1–a4), corresponding to the AA2024-T3, AA2198-T8, AA2198-T851, and AA7475-T761 alloys, the surface pores, indicated by white arrows, reveal the characteristic porosity of the anodic film formed by anodizing in an acidic solution.

Fig. 2 (b) shows the cross-sections of anodic films formed in defect-free regions. The measured film thicknesses were approximately 2.4 μm (AA2024-T3, (Fig. 2. (b1)), 2.6 μm (AA2198-T8, (Fig. 2. (b2)), 2.7 μm (AA2198-T851, (Fig. 2. (b3)), and 4.1 μm (AA7475-T761, (Fig. 2. (b3)). The variations in film thickness can be attributed to the density of IMPs present in the alloys. According to a recent study by our research group [113], the AA2024-T3 alloy has the highest population density of IMPs ($3472 \pm 157/mm^2$), covering 1.4 % of the surface area. In contrast, the AA7475-T761 alloy exhibits the lowest population density ($626 \pm 75/mm^2$), with only 0.14 % of the surface area covered by these particles. The AA2198-T8 and AA2198-T851 alloys show intermediate values, with surface area coverages of 0.25 % and 0.22 %, respectively. This suggests that a decrease in IMP density is associated with increased anodizing efficiency. According to the literature [120] the dissolution of high-copper-containing IMPs during anodizing consumes part of the electrical charge generated by the current, reducing efficiency and resulting in thinner films. This phenomenon explains the greater film thickness observed in the AA7475-T761 alloy compared to the others.

Fig. 2(c) presents cross-sections of the anodic films containing cavities formed during the anodizing process, caused by the dissolution of high-copper-containing IMPs. Fig. 2 (c1–c4) show these defect regions at lower magnification, while Fig. 2 (c5–c11) correspond to the areas highlighted by dashed squares, displayed at higher magnification. In these images, different types of defects are identified: surface cavity (SC), as seen in Fig. 2 (c5–c8), film/alloy interface cavity (FIC), and internal cavity (IC) within the film. In the AA7475-T761 alloy, certain regions of the anodic film contained occluded IMPs (Fig. 2 (c12)). The magnified view of region I (Fig. 2 (c13)) confirms the presence of these particles, with EDX analysis indicating approximately 4 wt% Cu,

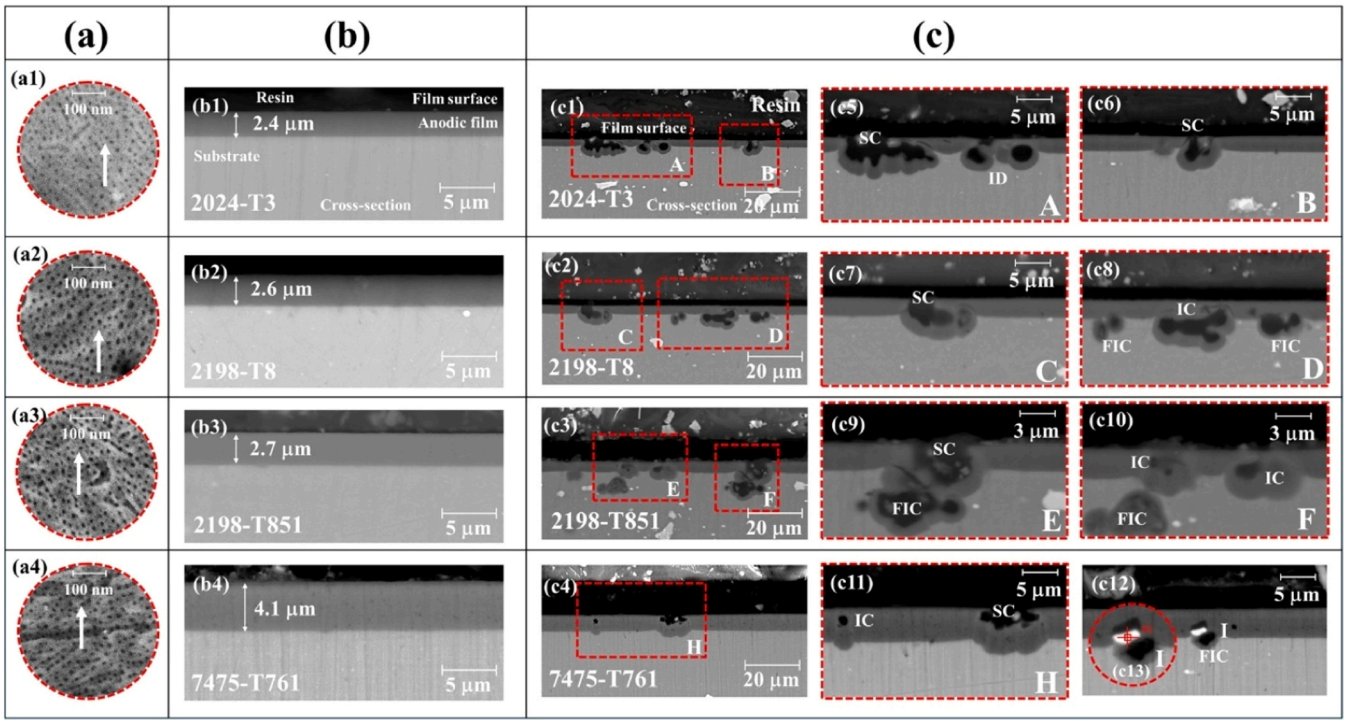

Fig. 2. Scanning electron micrographs of the tested anodized aluminium alloys: (a) surface of the anodic film; (b) cross-section of the films in defect-free regions; and (c) cross-section of the anodic films in regions with defects (cavities). Images (a1–a4) show the surfaces of the films corresponding to the tested alloys, (b1–b4) show the cross-sections of defect-free regions, and (c1–c4) show cross-sections in regions with defects at lower magnification. Images (c5–c11) provide higher magnification views of the dashed squares in (c1–c4); (c12) shows a coarse constituent intermetallic particle (IMP) occluded within the anodic film of the AA7475-T761 alloy; and (c13) shows a higher magnification of region I indicated in (c12). Labels SC, FIC, and IC in (c5–c12) denote surface cavity, film/alloy interface cavity, and cavity within the film, respectively. The images in (a) were acquired in secondary electron (SE) mode at an accelerating voltage of 5 kV, while those in (b) and (c) were acquired in backscattered electron (BSE) mode at an accelerating voltage of 20 kV.

confirming the presence of low-copper-containing IMP.

The findings (Figs. 1 and 2) demonstrate that the presence of IMPs during the anodizing process leads to the formation of defects, with their dimensions and locations determined by the distribution and composition of the particles in the alloy prior to anodization. The formation of FIC and IC-type defects indicates that not only surface defects should be considered, but also particles embedded within the alloy. The results suggest that the density, size, location, and composition of the IMPs are critical factors in the development of these ones. Therefore, these aspects should be thoroughly investigated for their impact on the corrosion resistance of the anodized aluminium alloys, as will be discussed in the following sections.

3.2. Corrosion assessment of anodized alloys: surface characterization

Fig. 3 presents optical micrographs illustrating the surface morphology of various anodized aluminium alloys after immersion in 0.1 mol L^{-1} NaCl solution for 24 h.

The initial analysis of all alloys (Fig. 3 (a-d)) shows the formation of dispersed black spots on the surfaces of the anodized films, preliminarily identified as indicators of localized corrosion sites. At higher magnification (Fig. 3 (a1-d1)), these black spots display circular features, as

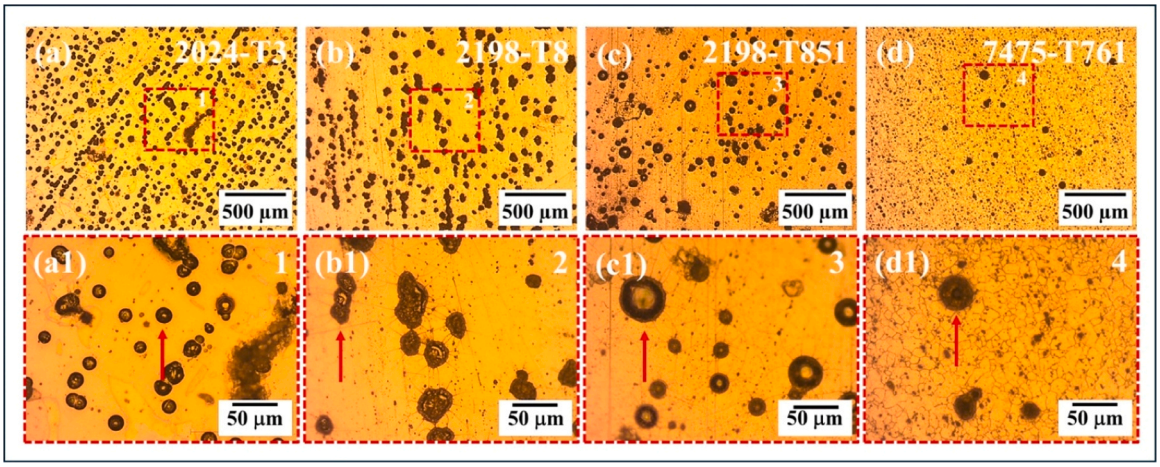

Fig. 3. Optical micrographs of the surface of anodized aluminium alloys after immersion in 0.1 mol L^{-1} NaCl solution for 24 h: (a–d) surfaces of the samples at lower magnification; (a1–d1) higher magnification of the dashed areas in (a–d). Red arrows indicate some locations associated with localized corrosion.

indicated by the red arrows. The statistical data of the black spots are presented in Table 3.

The AA2024-T3 alloy (Fig. 3 (a)) exhibited the highest population of circular localized corrosion sites, corresponding to 255 ± 29 per unit area (μm^2) with an average diameter of 20.5 ± 9.2 μm, indicating high susceptibility to corrosion.

The Al-Cu-Li alloys, AA2198-T8 (Fig. 3 (b)) and AA2198-T851 (Fig. 3 (c)), showed intermediate numbers of corrosion sites, 150 ± 16 and, 140 ± 14/μm^2, respectively. In contrast, the AA7475-T761 alloy (Fig. 3 (d)) displayed the lowest population of the corrosion sites, corresponding to 79 ± 7/μm^2 and with the smallest average diameter, (15.1 ± 2.7) μm. Both alloys exhibited similar average diameter of the circular corrosion sites, (21.3 ± 2.5) μm, indicating moderate susceptibility to localized corrosion relatively to the other alloys studied.

These findings are further supported by SEM analysis, as shown in Fig. 4, which provides additional insight into the corrosion sites. The observation of these localized corrosion sites at high magnification reveals not only their size and distribution but also their typical morphology.

Fig. 4 (a–d) illustrates the distribution of corrosion sites on the anodic film surfaces of the aluminium alloys, as previously highlighted in Fig. 3. Fig. 4 (a1–d1) presents higher-magnification views of the dashed areas shown in Fig. 4 (a–d), revealing the details of circular corrosion sites that correspond to weakened regions of the anodic film. These pits appeared after immersion in NaCl solution, suggesting points of increased susceptibility to corrosion. The corresponding EDX maps (Fig. 4 (a2-d2)) show a localized concentration of copper (Cu), which may be attributed to the underlying matrix exposed due to corrosion processes, suggesting that the anodic film was compromised in these regions. Additionally, the absence of iron (Fe) in the EDX maps of these areas confirm that these regions are not associated with remnant intermetallic particles, as evidenced by the absence of Fe signals. This finding indicates that the presence of Cu in these regions is not related to constituent intermetallic particles. Additionally, the detection of chloride (Cl) at these sites suggests that they serve as preferential locations for localized corrosion attack.

To investigate and evaluate these different theories, immersion tests were conducted, monitoring defect formation from its early stages, and correlating these defects with the initiation of localized corrosion, as illustrated in Fig. 5 (a-d) that presents the polished surfaces of the alloys at lower magnification, where the distribution of IMPs can be observed.

Fig. 5 (a1-d1) are magnified views of the dashed areas in Fig. 5 (a-d), and the IMPs are indicated by red arrows.

After anodizing, the alloy surfaces are shown in Fig. 5 (a2-d2), revealing morphological changes caused by the partial or total dissolution of the IMPs. The magnified views of these areas are presented in Fig. 5 (a3-d3), where cavities resulting from the dissolution of IMPs are indicated by white arrows, representing defects in the surface of the anodic films. Fig. 5 (a4-d4) displays the anodized surfaces after immersion in 0.1 mol L^{-1} NaCl solution for 24 h. Despite exposure to the saline solution, the magnified views of the dashed areas (Fig. 5 (a5-d5)) do not reveal signs of corrosion in the defective areas of the anodic film, as previously seen in Figs. 3 and 5. However, circular pits were detected in areas without surface defects (Fig. 5 (a4-d4)), as indicated by the blue dashed-line squares A-D. These regions were analysed in high magnification and are presented in Fig. 6.

Fig. 6 (a-d) depict circular localized corrosion sites observed in all alloys following immersion, which were analysed to investigate the progression of corrosion beneath them. To facilitate this analysis, the anodic film was stripped in these regions, as shown in Fig. 6 (a1-d1), exposing the localized corrosion sites in the alloy substrate beneath. The images obtained in SE mode of the same regions (Fig. 6 (a2-d2)) provide clearer evidence of the localized corrosion pits, with diameters in the range from 7 μm to 16 μm. Notably, the dimension and shape of these sites on anodic film surface (Fig. 6 (a-d)) are similar to with the size and shape of the corrosion pits (Fig. 6 (a1-d1)). This suggests that the circular features observed after immersion are a consequence of corrosion processes originating from pre-existing defects within the anodic film. These defects, although initially present and not detectable by SEM from the surface, were revealed in cross-sectional analysis, as shown in Fig. 2, and served as initiation sites for localized corrosion. Previous studies [29,36] have demonstrated that these pits (Figs. 4, 5, and 6) predominantly correspond to localized corrosion sites in the alloy substrate beneath the anodic film, as confirmed after film stripping (Fig. 6 (a1-d2)).

The findings indicate (Fig. 5) that defects that appear at the surface of the anodic film but do not extend to the film/substrate interface do not significantly diminish the overall corrosion resistance of the alloys. However, as shown in Fig. 5, localized corrosion sites (Fig. 6) developed far from the surface defects identified after anodizing, which were induced by IMP dissolution. This distribution limited the ability to precisely monitor corrosion in both defective and non-defective regions simultaneously. Therefore, a shorter immersion period (12 h) in 0.1 mol L^{-1} chloride solution was employed on a high-magnification region containing both surface defects and defect-free areas, enabling a more detailed observation of the initiation of the corrosion process, as presented in Fig. 7.

Fig. 7 (a-d) shows the surfaces of aluminium alloys before anodizing, with the IMPs indicated by white arrows. Following the anodizing process, the dissolution of the IMPs leads to the formation of defects at the surface film, as reported in Fig. 1, and as indicated by the red arrows in Fig. 7 (a1-d1). The areas highlighted by the dashed squares A-D correspond to regions free of IMPs, which consequently did not exhibit surface defects after anodizing, as shown in Fig. 7 (a1-d1).

Nevertheless, after 12 h of immersion in 0.1 mol L^{-1} NaCl solution, the areas of the oxide film with defects at the surface (Fig. 7 (a1-d1)) did not show evidence of corrosion initiation. In contrast, the regions initially free of surface defects (squares A-D) developed circular corroded sites on the oxide surface. The magnified views of these regions (Fig. 7 (a3-d3)) confirm the formation of localized corrosion sites (indicated by the yellow arrows) and changes in the composition of the film in these areas. After film stripping (Fig. 7 (a4-d4)), cavities with diameters ranging from 5 to 10 μm were observed beneath the film (indicated by the blue arrows).

The findings presented in Figs. 6 and 7 indicate that the localized corrosion sites in the anodic film are closely linked to the defects beneath the film. Additionally, the immersion duration in the NaCl solution significantly affects the size of these cavities and, consequently, their final size. Fig. 8 illustrates that longer immersion periods result in larger cavities, establishing a relationship between exposure duration and the progression of corrosion.

Fig. 8 (a-d) shows the surfaces of aluminium alloys after 48 h of immersion in 0.1 mol L^{-1} NaCl solution, followed by film stripping, which reveals circular features on the alloy substrate. The scanning electron micrographs indicate the presence of cavities in the substrate associated with localized corrosion. The magnified views of the regions highlighted by dashed squares in Fig. 8 (a1-d1) confirm the presence of

Table 3
Statistical data on the characteristics of the localized corrosion sites (Fig. 3) observed in the anodized aluminium alloys after immersion testing in 0.1 mol L^{-1} NaCl solution for 24 h.

Features after 24 h of immersion	Aluminium Alloys			
	AA2024-T3	AA2198-T8	AA2198-T851	AA7475-T761
Population (per unit area (μm^2))	255 ± 29	150 ± 16	140 ± 14	79 ± 7
Diameter (μm)	20.5 ± 9.2	21.3 ± 2.5	21.3 ± 2.5	15.1 ± 2.7

* The calculation was performed randomly over an area of 3×2.5 mm^2, using 20 images.

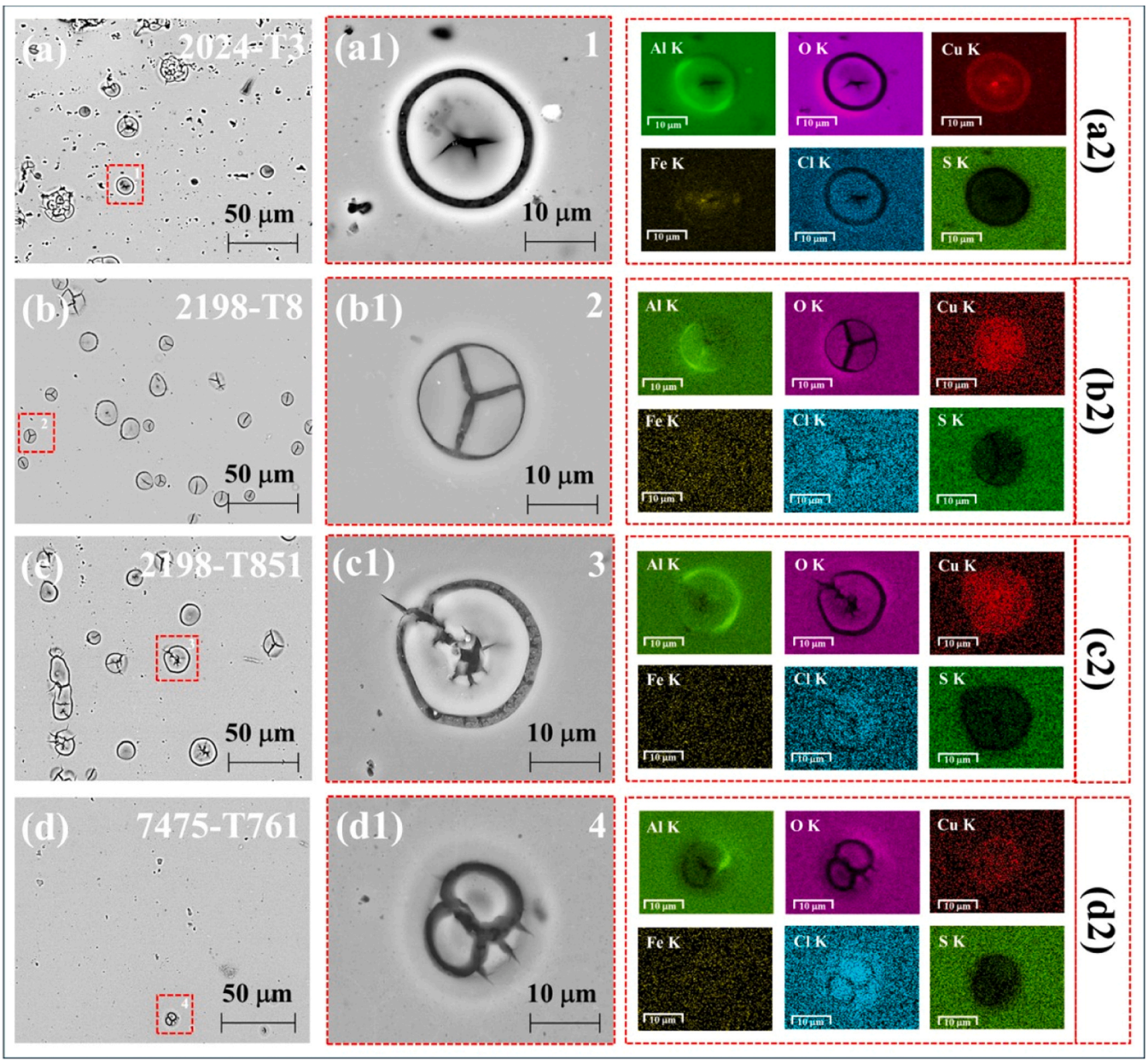

Fig. 4. Scanning electron micrographs of the surface of anodized aluminium alloys after immersion in 0.1 mol L^{-1} NaCl solution for 24 h: (a–d) surfaces at lower magnification; (a1–d1) higher magnification of the dashed squares in (a–d); and (a2–d2) EDX maps corresponding to (a1–d1). All images were acquired in back-scattered electron (BSE) mode at an accelerating voltage of 20 kV.

these cavities. In Fig. 8 (a2-d2) and (a3-d3), the circular cavities have diameters ranging from 30 to 40 µm, which are larger than those observed after shorter immersion times (Fig. 7 (a2-d2) and (a4-d4)), suggesting that corrosion intensifies with developed with time. In particular, for the AA7475 alloy, as indicated by the white arrow in Fig. 8 (d2), intergranular corrosion (IGC) can be observed within the circular pit, indicating a susceptibility of ICG attack in this region.

Fig. 8 (a4-d4) and (a5-d5) shows higher magnification comparisons of the aluminium substrate in regions without cavities (Fig. 8 (a4-d4)) and within the cavities (Fig. 8 (a5-d5)). In the areas without cavities, the substrate displays a scalloped surface, while within the cavities, the structure appears rougher indicating aggressive corrosion in these regions. The morphological differences between Fig. 8 (a4-d4) and (a5-d5) suggest that the corrosive solution penetrated predominantly the defective areas, whereas most area of the substrate alloy remained intact likely due to the barrier of anodic film that denied access of the corrosive solution. Another aspect to be noted is that, for longer immersion times, the circular corrosion sites formed beneath the anodic film acted as sites for the initiation of crystallographic attack in all alloys, as illustrated in Fig. 9.

Fig. 9 presents scanning electron micrographs of aluminium alloys after anodizing, followed by immersion in 0.1 mol L^{-1} NaCl solution for 60 h and subsequent film stripping. At lower magnification, (Fig. 9 (a-d)), it is seen that significant cavities formed because of the corrosive process. At higher magnifications, within the dashed areas in Fig. 9 (a-d), a more pronounced attack within the cavities is evident. The dashed circles in Fig. 9 (a2-d2) highlight regions A-D from Fig. 9 (a1-d1), were, as indicated by the white arrows, crystallographic attack within the cavities can be seen. These findings suggest that pits with circular characteristics, formed as a result of localized corrosion, represent areas of increased vulnerability. This could potentially lead to further corrosion propagation and compromise the integrity of the anodized alloy

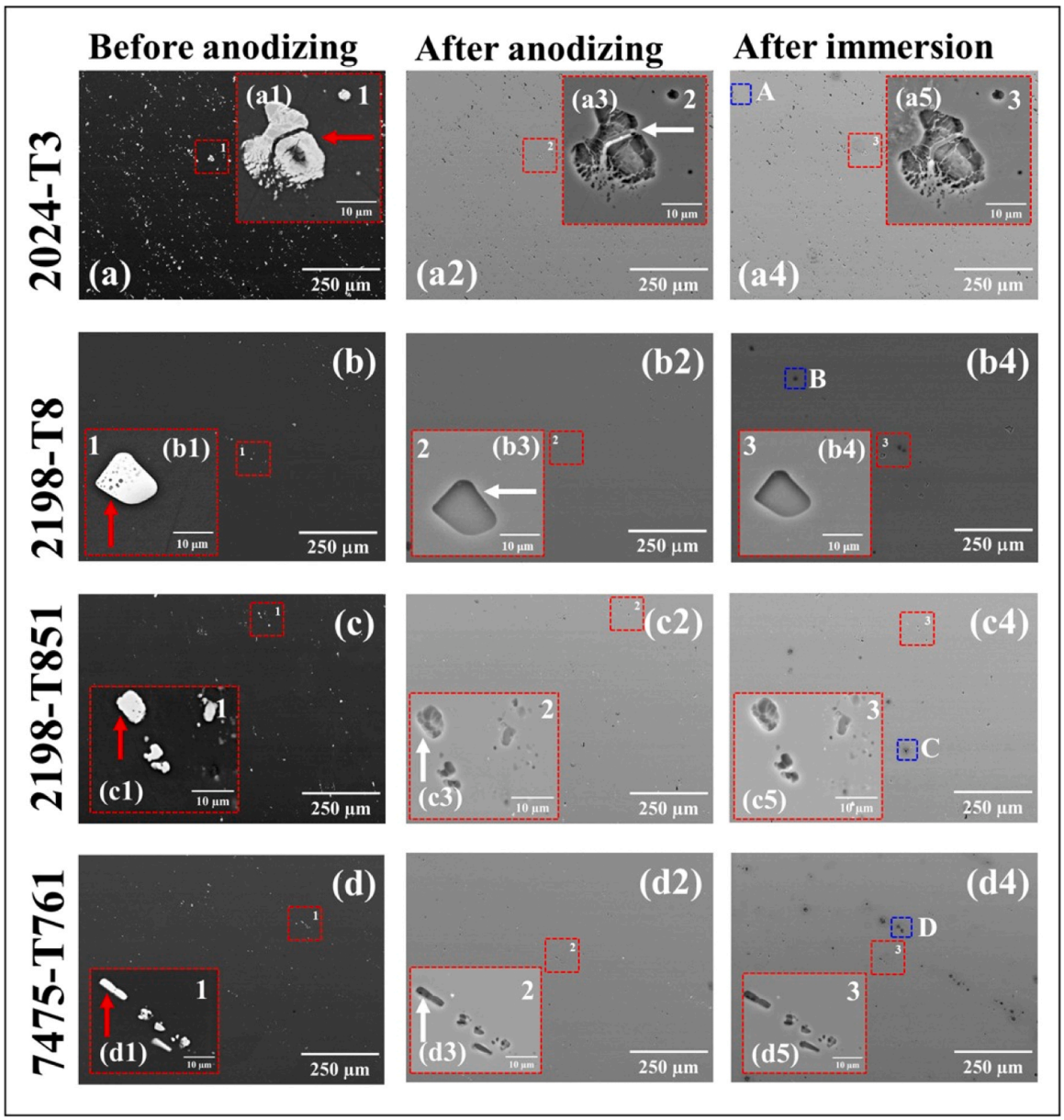

Fig. 5. Scanning electron micrographs of aluminium alloys: (a–d) surfaces before anodizing; (a1–d1) higher magnification of the dashed squares in (a–d); (a2–d2) surfaces after anodizing; (a3–d3) higher magnification of the dashed squares in (a2–d2); (a4–d4) surfaces after immersion in 0.1 mol L^{-1} NaCl solution for 24 h; (a5–d5) higher magnification of the dashed squares in (a4–d4). All images were acquired in backscattered electron (BSE) mode at an accelerating voltage of 20 kV. Red arrows indicate constituent intermetallic particles on the surface, while white arrows point to defects on the oxide surface caused by dissolution of IMPs during the anodizing process.

under service conditions.

According to the literature [121,122], crystallographic attack is favoured by aggressive chemical conditions inside the cavities, such as low pH and high chloride ion concentration. Crystallographic defects within the alloy matrix act as nucleation points for this type of attack. Previous studies on the AA2055 Al-Cu-Li alloy suggested that cavities could act as initiation sites for this type of corrosion, although a direct correlation was not established [29]. However, in the present work, it was clearly demonstrated that cavities indeed serve as preferential sites for the initiation of crystallographic corrosion in the alloys studied.

The results presented in Figs. 5, 6, and 7 appear to contradict earlier studies that proposed that corrosion initiates at surface defects in the anodic film [11–13,16,28,34,35]. However, these findings are consistent with research on other aluminium alloys, such as AA2099 [36] and AA2055 [29,37], which indicates that defects within the anodic film, or at the film/alloy interface, play a critical role in localized corrosion. This indicates that corrosion mechanisms are not governed by surface defects but are significantly influenced by the integrity of the subsurface film. To further substantiate this hypothesis, a detailed cross-sectional analysis of both regions, corroded and non-corroded, is required, as discussed in the following section.

3.3. *Assessing corrosion in anodized alloys: cross-sectional analysis*

Fig. 10 presents the cross-sectional analysis of the anodized alloys at locations exhibiting pits in the anodic film, following a 24 h immersion test in 0.1 mol L^{-1} NaCl solution.

Fig. 10 (a-d) shows circular pits formed on the surface of the aluminium alloys by immersion in NaCl. Fig. 10 (a1-d1) shows the same pits tilted at a 30° angle where cracks and protrusions in the anodic film

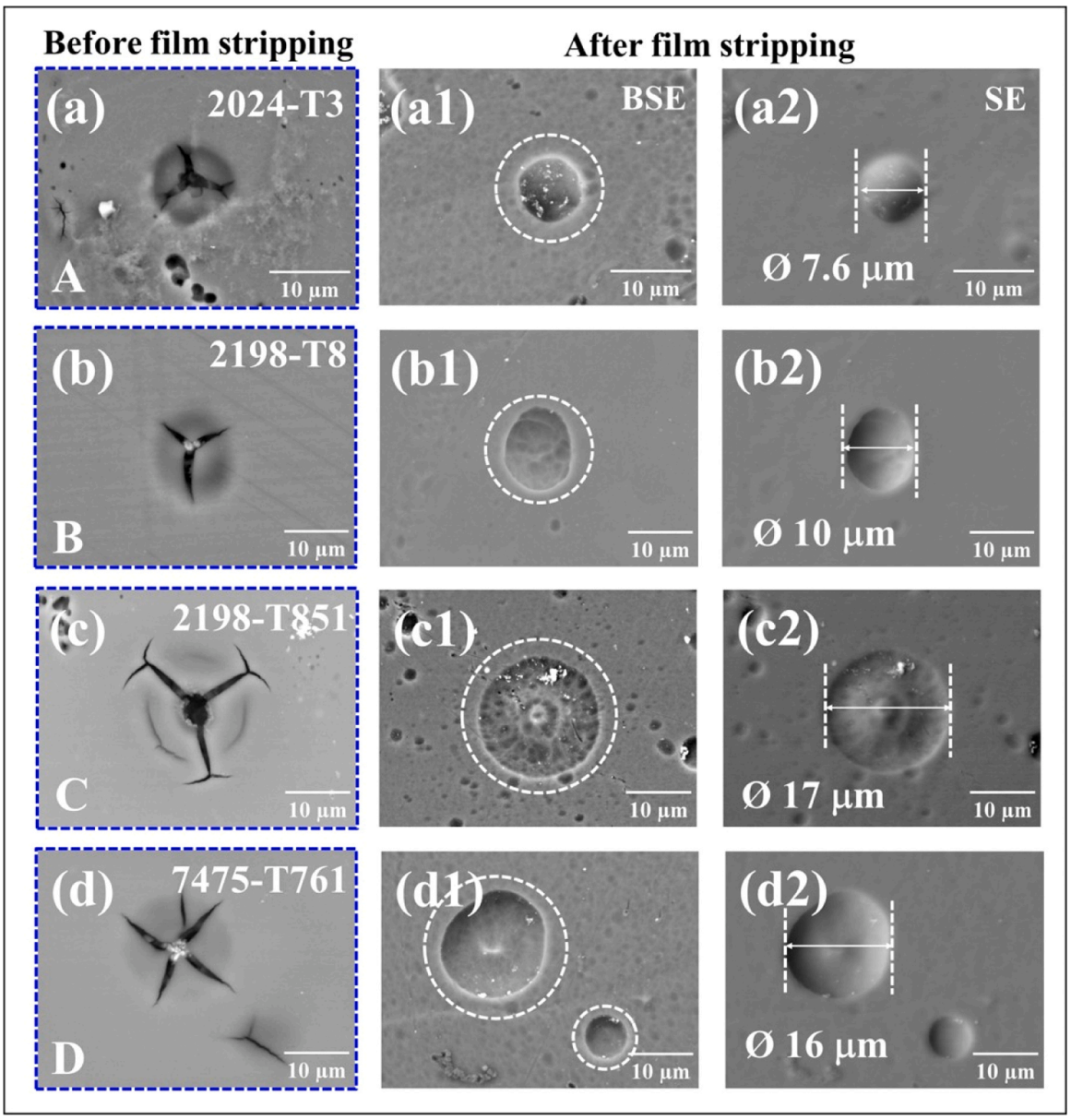

Fig. 6. Scanning electron micrographs of the surface of anodized aluminium alloys after immersion in 0.1 mol L^{-1} NaCl solution for 24 h: (a–d) higher magnification of the dashed squares in Fig. 5 (a4–d4); (a1–d1) images obtained after film stripping using backscattered electrons; and (a2–d2) images obtained using secondary electrons.

are seen in result of corrosion. Specifically, Fig. 10 (a) and (b) reveal a higher number of cracks in the regions adjacent to the circular attacked regions, likely caused by the contraction of the material due to dehydration of the film after the immersion test and subsequent drying. Fig. 10 (a2-d2) presents the EDX maps corresponding to these pits, where a significant concentration of elements, such as copper, is observed.

The cross-sections obtained by ultramicrotomy, shown in Fig. 10 (a3-d3) and 10 (a4-d4), provide a detailed analysis of the internal structure of the circular pits. Fig. 10 (a3-d3) correspond to the C1 cut, made at the initial edge of the pit, which highlights the morphology of the pits in cross-section, while Fig. 10 (a4-d4) represents the C2 cut, extending deeper toward the centre of the pits. In the C1 cut, Fig. 10 (a3-d3) reveals the edge of the pits, highlighting discontinuities in the anodic film. However, for the AA2024-T3 alloy (Fig. 10 (a3)), associated with the C1 cut, this phenomenon was not clearly observed, possibly because the section was not close enough to reveal the onset of the cavity, an aspect to be discussed later. As the sections progress, the pits become deeper and acquire circular characteristics, as shown in the C2 cut (Fig. 10 (a4-d4)), consistent with the surface analyses (Figs. 5 and 9).

In Fig. 10 (a5-d5), which correspond to the EDX maps of the cross-sections, a significant concentration of chlorine is observed in the corroded regions, indicating localized attack. Moreover, in some pits, there is a notable presence of copper, as shown in the surface maps (Fig. 10 (a2-d2)).

For a more detailed analysis of the corrosion-associated regions, Fig. 11 provides a higher magnification of the dashed squares in Fig. 10 (a3-d3) and (a4-d4), corresponding to the C1 and C2 cuts.

Fig. 11 (a-d) provides higher magnification views of the highlighted areas from Fig. 11 (a3-d3), showing the edges of cavities and evidence of substrate attack in the Al-Cu-Li and AA7475-T761 aluminium alloys. The cavity depths measured range from 0.8 µm to 1.6 µm. These measurements were taken between yellow dashed lines indicating the anodic film/alloy and cavity/alloy interfaces, providing precise delineation of corrosion progression relative to the substrate. In the higher magnification images of Fig. 11 (a1-d1), substrate attack is clearly

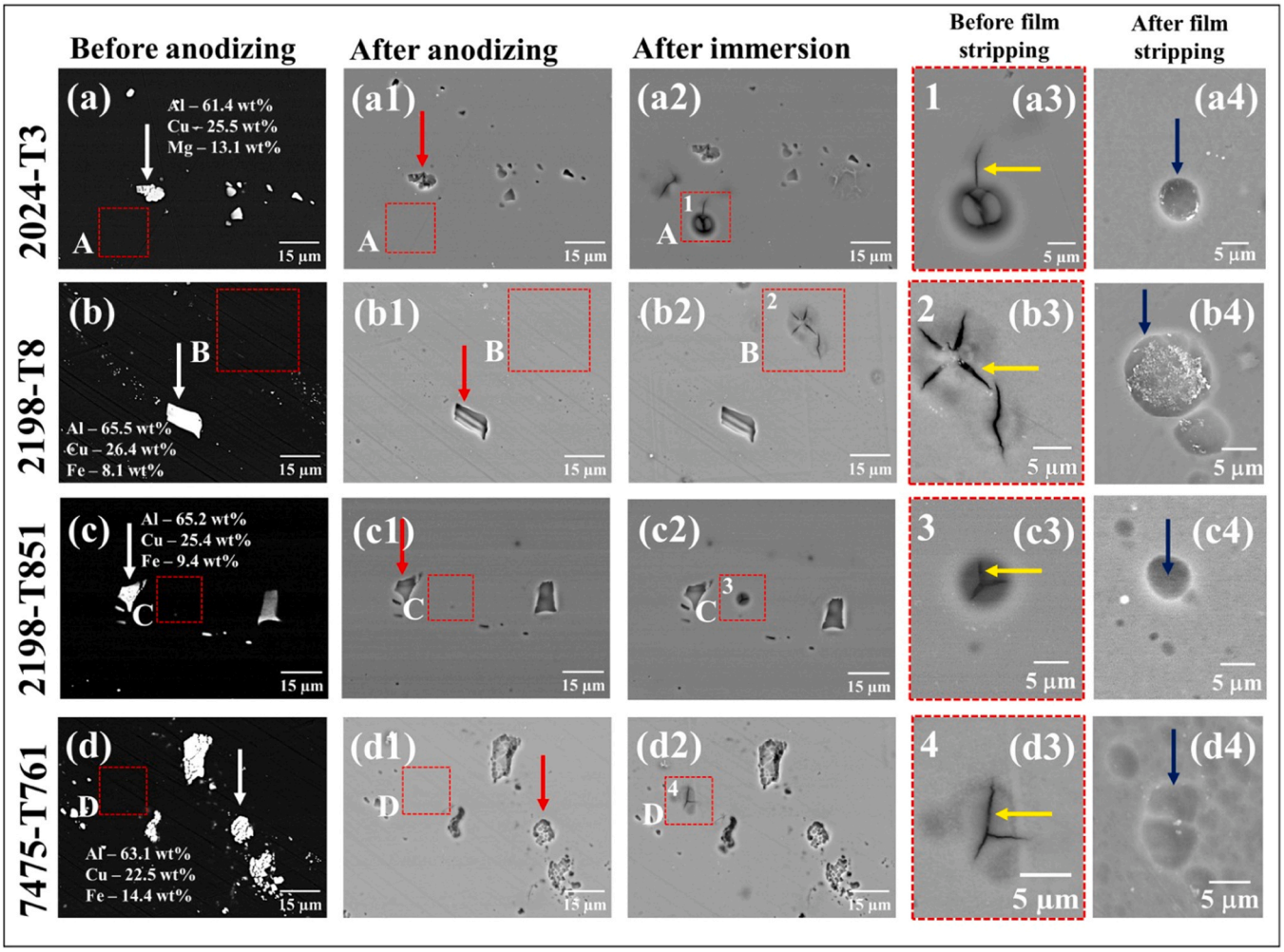

Fig. 7. Scanning electron micrographs of aluminium alloys: (a–d) surface before anodizing; (a1–d1) surface after anodizing; (a2–d2) surface after immersion in 0.1 mol L^{-1} NaCl solution for 12 h; (a3–d3) higher magnification of the dashed squares in (a2–d2); and (a4–d4) surface shown in (a3–d3) after film stripping. All images were acquired in backscattered electron (BSE) mode at an accelerating voltage of 20 kV. Yellow arrows indicate cracks formed in the anodic oxide, while blue arrows point to cavities beneath the anodic film.

visible, as indicated by red arrows. In the AA2024-T3 alloy (Fig. 11 (a1)), cavity initiation was not observed, likely due to ultramicrotome cutting away from the pit edge. Nonetheless, an anodic film detachment at the film/alloy interface (marked by a red arrow) indicates corrosion at this interface, suggesting localized attack.

Fig. 11 (e-h) provides a closer look at the areas highlighted in Fig. 11 (e4-d4), which correspond to the C2 section. These images show an increase in cavity depth, ranging from 4 µm to 6 µm, as the section was taken from the centre of the pit, where the cavity is deeper. This result suggests that the cross sections obtained near the pit edges (as shown in Fig. 11 (a1-d1)) were relatively shallow compared to those closer to the centre of the pit. The higher magnification images in Fig. 11 (e1-h1) clearly display the ongoing attack on the substrate, revealing the extent of corrosion below the film/alloy interface. The depth and morphology of the cavities indicate significant progression of the corrosion process in the analysed alloys.

The results reported in Figs. 10 and 11 provide important evidence of under film corrosion, suggesting that corrosion initiates at points where film defects lead to localized attack at the centre of the circular corrosion site (Fig. 10 (a4-d4)). From this initiation point, corrosion propagates both inwards and laterally, forming semi-spherical pits (Fig. 11 (e-h)). Notably, lateral propagation may also occur in defect-free areas of the film, as illustrated in Fig. 10 (a1).

The difference in brightness and contrast between the initial film, the film modified by corrosion, and the corrosion products further corroborates these observations, highlighting the evolution of the degradation process. The results in Figs. 10 and 11 suggest that the absence of film above the cavities is likely due to oxide detachment, which occurs as a consequence of the weakened oxide film in corroded regions. This detachment obscures a clear view of the corrosion characteristics at the film/alloy interface. Consequently, more precise ultramicrotomy cuts near the pits are necessary for a detailed examination of this interface. Given that previous studies on AA2055 [29] and AA2099 [36] alloys did not use this methodology, applying these precise cuts is essential to further elucidate the localized corrosion mechanism.

Precise cross-sectional cuts were performed, as shown in Fig. 12, focusing on a representative pit selected for detailed analysis. This pit was chosen as it reflects the typical corrosion pattern observed across all alloys (Fig. 4), with pits forming on the oxide surface. By analysing this specific corrosion site, the main mechanisms contributing to this type of degradation can be better understood.

Fig. 12 (a) shows a scanning electron micrograph of the surface of one of the aluminium alloys after anodizing and subsequent immersion in a 0.1 mol L^{-1} NaCl solution for 24 h. The dashed lines C1 to C4 correspond to the precise ultramicrotomy cuts made in the region of localized attack. Fig. 12 (b) presents the cross-sectional view corresponding to cut C1, which shows no indications of corrosive attack on the alloy substrate, as it is located far from the cavity region and displays

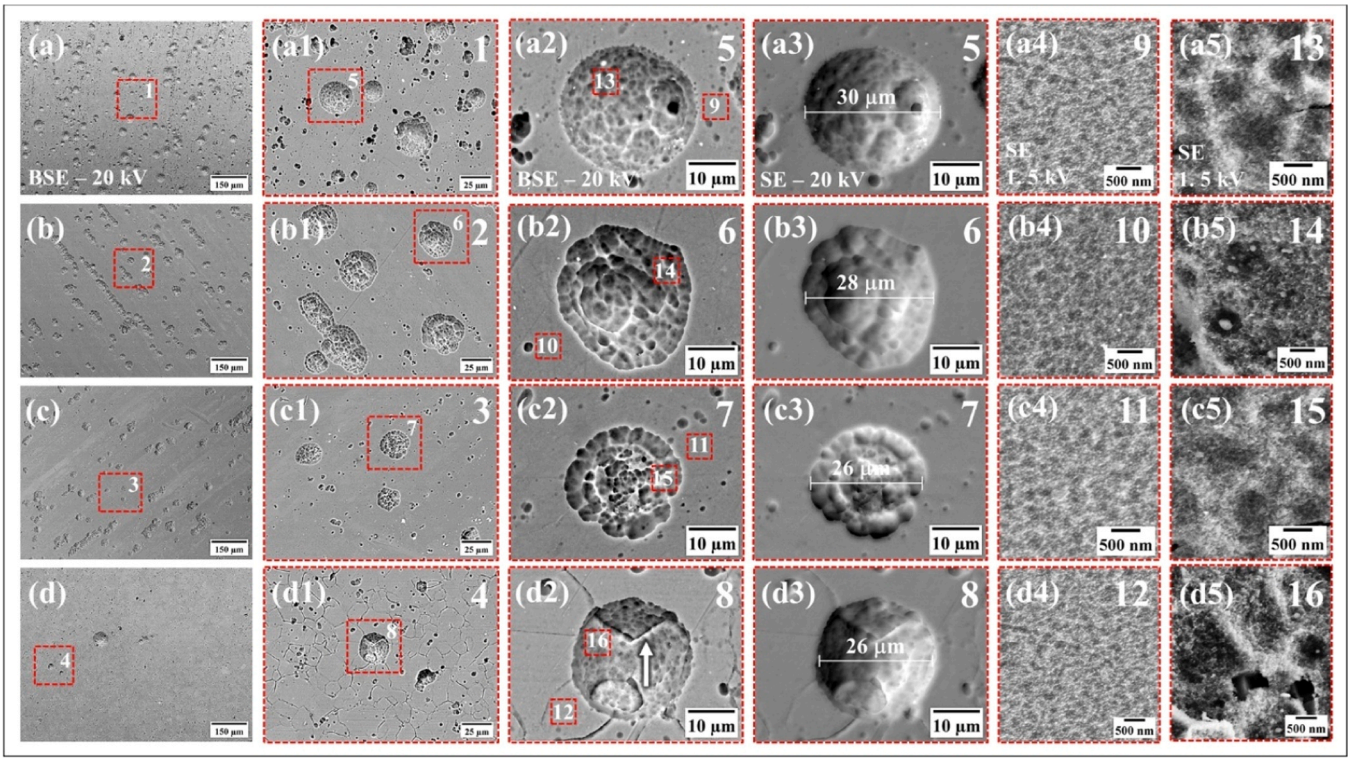

Fig. 8. Scanning electron micrographs (SEM) of aluminium alloys after anodizing after immersion in 0.1 mol L^{-1} NaCl solution for 48 h and subsequent film stripping: (a–d) surface images at lower magnification; (a1–d1) higher magnification of the dashed areas in (a–d); (a2–d2) higher magnification of the dashed areas in (a1–d1); (a3–d3) higher magnification of the dashed areas in (a2–d2); and (a4–d4) higher magnification of the dashed areas in (a3–d3). Images (a–d2) were acquired in backscattered electron (BSE) mode at an accelerating voltage of 20 kV; images (a3–d3) in secondary electron (SE) mode at 20 kV; and images (a4–d4) in SE mode at 1.5 kV. The white arrow in (d2) indicates the presence of intergranular corrosion (IGC).

only the anodic film in a corrosion-free area.

As the cut approach the corroded region (Fig. 12 (a)), evidence of corrosive attack begins to emerge. Fig. 12 (c) shows the cross-section of cut C2, which is slightly distant from the centre of the pit (corresponding to the pit edge). A discontinuity is observed at the film/alloy interface, suggesting corrosion of the alloy substrate. Above this discontinuity is a region of the anodic film with a darker coloration in a semi-elliptical shape. Fig. 12 (c1) and (c2) show the highlighted region 1 from Fig. 12 (c) at higher magnification, with the yellow dashed line (Fig. 12 (c2)) indicating the film/alloy interface.

SE mode images (Fig. 12 (c2)) between the region without dark coloration (blue dashed circle) and the region with dark coloration (yellow dashed circle) confirm that the morphology of the anodic film is the same in both areas. This indicates that the dark coloration is not due to morphological changes in the anodic film that may occur during its formation, thus eliminating this factor as a cause of the observed contrast differences. Additionally, there is no evidence of damage caused by the ultramicrotomy process in either region, further dismissing the possibility that the observed contrast is an artifact from the cutting process.

The contrast difference indicated by the yellow arrow in Fig. 12 (c1) is attributed to the modification of the anodic film due to the absorption of corrosion products, confirming that the discontinuity indicated by the red arrow corresponds to the corroded substrate. Similar results have been reported in previous studies on anodized aluminium alloys after immersion tests in chloride-containing solutions [29,36,37]. The modification of the film is associated with corrosion events in the alloy substrate beneath the film, which explains the contrast differences observed in regions of localized corrosion compared to the adjacent oxide surface, as illustrated in Figs. 6 and 7.

Distinguishing the modified anodic film from the unmodified one by means of SEM analysis is a challenging task, as the porous film hydrates after immersion testing, altering the Al atomic ratio from 2:3 (Al_2O_3) to approximately 1:2–3 ($Al(OH)_3$/AlO(OH)), similar to corrosion products [123]. Therefore, the Al ratio cannot be used to differentiate them. Additionally, corrosion products may contain other species, such as Cl, which EDX cannot detect at concentrations below 0.1 % [124]. The limited spatial resolution of EDX in SEM, at the micrometer scale, also means that the results reflect the average value of the entire sampling volume (approximately) 1–3 μm^3 [124–126]. The observed contrast difference is explained by the absorption of corrosion products with higher atomic weight, making the modification of the anodic film more evident. Thus, the most effective way to observe this contrast difference is through SEM in BSE mode, which is sensitive to variations in atomic weight, allowing identification of the regions of the film that have been modified by corrosion processes.

In Fig. 12 (c1), the distance between the corroded region, indicated by the purple arrow, and the beginning of the anodic film is less than 1 µm. This is because cut C1 was made at the edge of the pit (Fig. 12 (a)), which has a spherical morphology and is shallower at the edges, as reported in Fig. 11 (a-d), becoming deeper toward the centre.

Fig. 12 (d) shows the images corresponding to cut C3. The discontinuity observed in the anodic film above the cavity may result from film detachment during the cutting process, as reported in Figs. 10 and 11. This hypothesis is supported by the presence of film fragments, indicated by the white arrows. In fact, as previously mentioned, the region containing the modified anodic film becomes weakened due to the absorption of corrosion products and the volumetric contraction caused by them, which can lead to oxide detachment during ultramicrotomy cutting.

The circular cavity (Fig. 12 (d)) becomes more evident below the film/alloy interface, as indicated by the yellow dashed line. The measured distance between the cavity and the film/alloy interface was 1.2 µm, indicating a greater depth of attack compared to cut C1 (Fig. 12

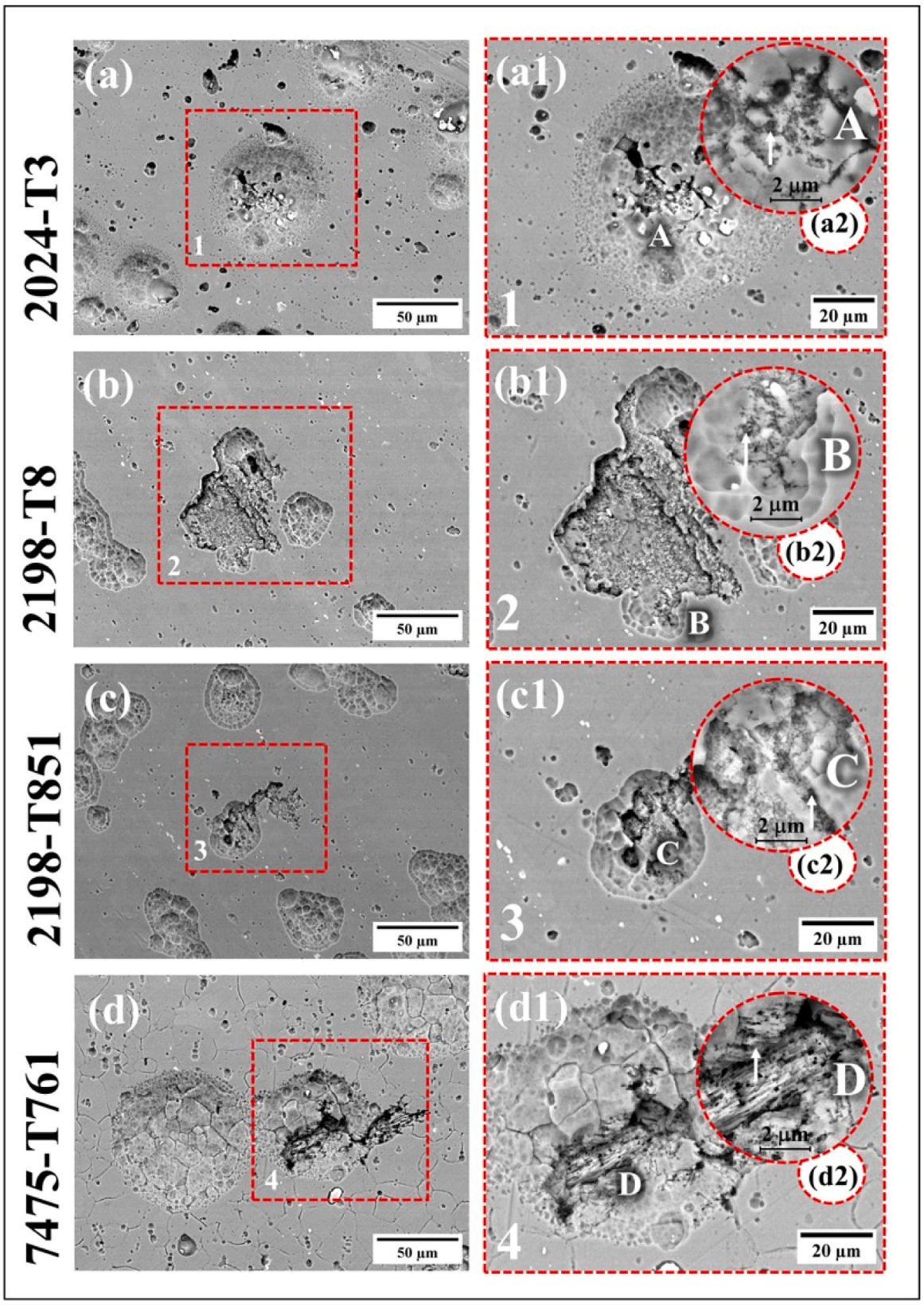

Fig. 9. Scanning electron micrographs of the surface of anodized aluminium alloys after immersion in 0.1 mol L^{-1} NaCl solution for 60 h and subsequent film stripping: (a–d) surface at lower magnification; (a1–d1) higher magnification of the dashed squares in (a–d); (a2–d2) higher magnification of regions A–D highlighted in (a1–d1). White arrows in (a2–d2) indicate crystallographic etching within the cavities. All images were acquired in backscattered electron (BSE) mode at an accelerating voltage of 20 kV.

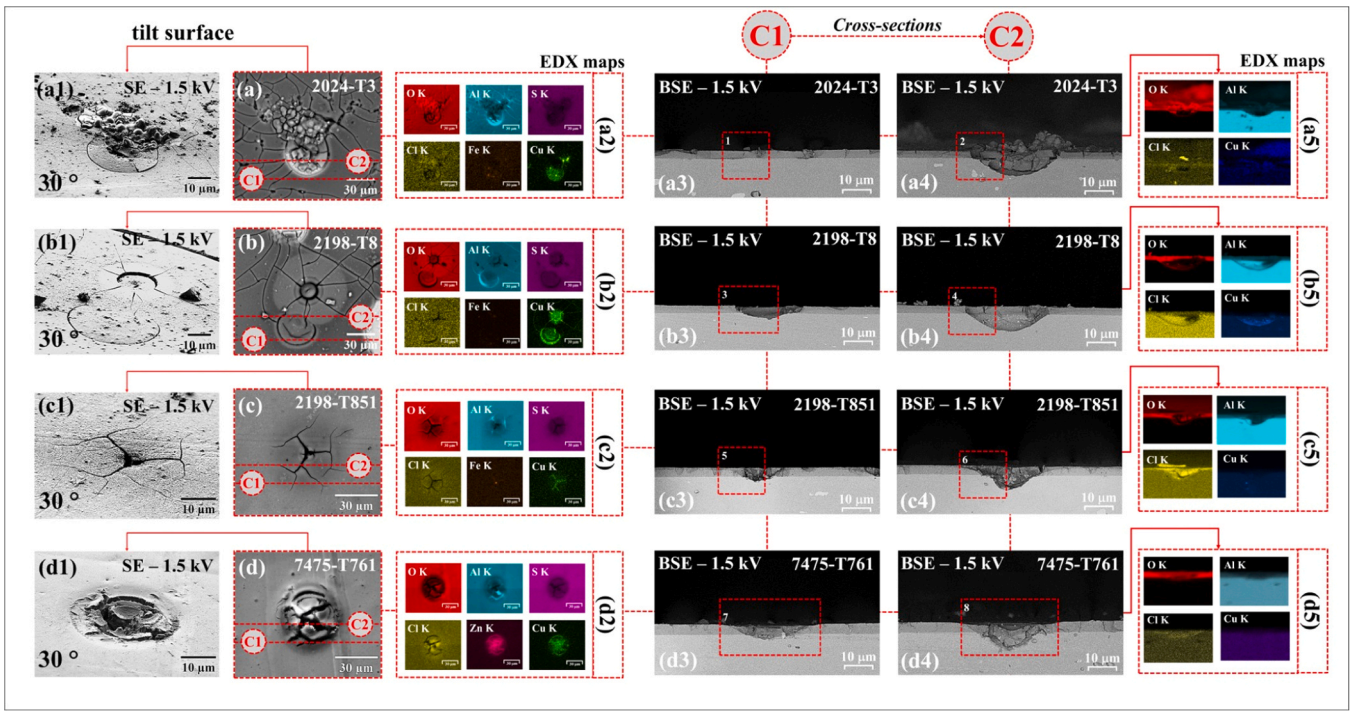

Fig. 10. Scanning electron micrographs of aluminium alloys after anodizing and subsequent immersion in 0.1 mol L^{-1} NaCl solution for 24 h: (a–d) images showing localized corrosion sites (pits) formed after immersion; (a1–d1) pits corresponding to images (a–d) with the surface tilted at a 30° angle; (a2–d2) EDX maps corresponding to (a–d); (a3–d3) cross-sectional cuts C1 of the pits in (a–d); (a4–d4) cross-sectional cuts C2 of the pits in (a–d); and (a5–d5) EDX maps of the cross-sections of the pits in (a4–d4).

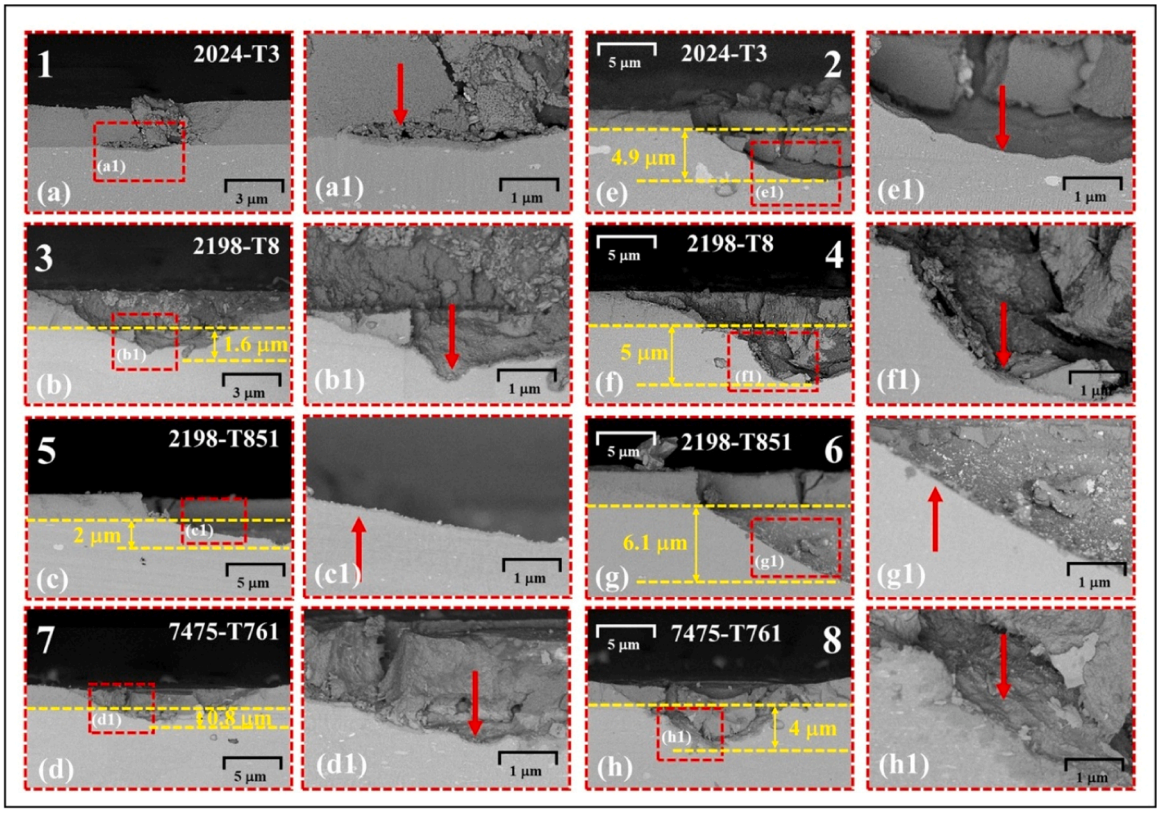

Fig. 11. Scanning electron micrographs of the surface of anodized aluminium alloys after immersion in 0.1 mol L^{-1} NaCl solution for 24 h: (a–d) higher magnification of the dashed squares in Fig. 10 (a3–d3); (a1–d1) higher magnification of the dashed squares in (a–d); (e–h) higher magnification of the dashed squares in Fig. 10 (a4–d4); (e1–h1) higher magnification of the dashed squares in (e–h). All images were acquired in backscattered electron (BSE) mode at an accelerating voltage of 1.5 kV. Red arrows in (a1–h1) indicate the corroded substrate.

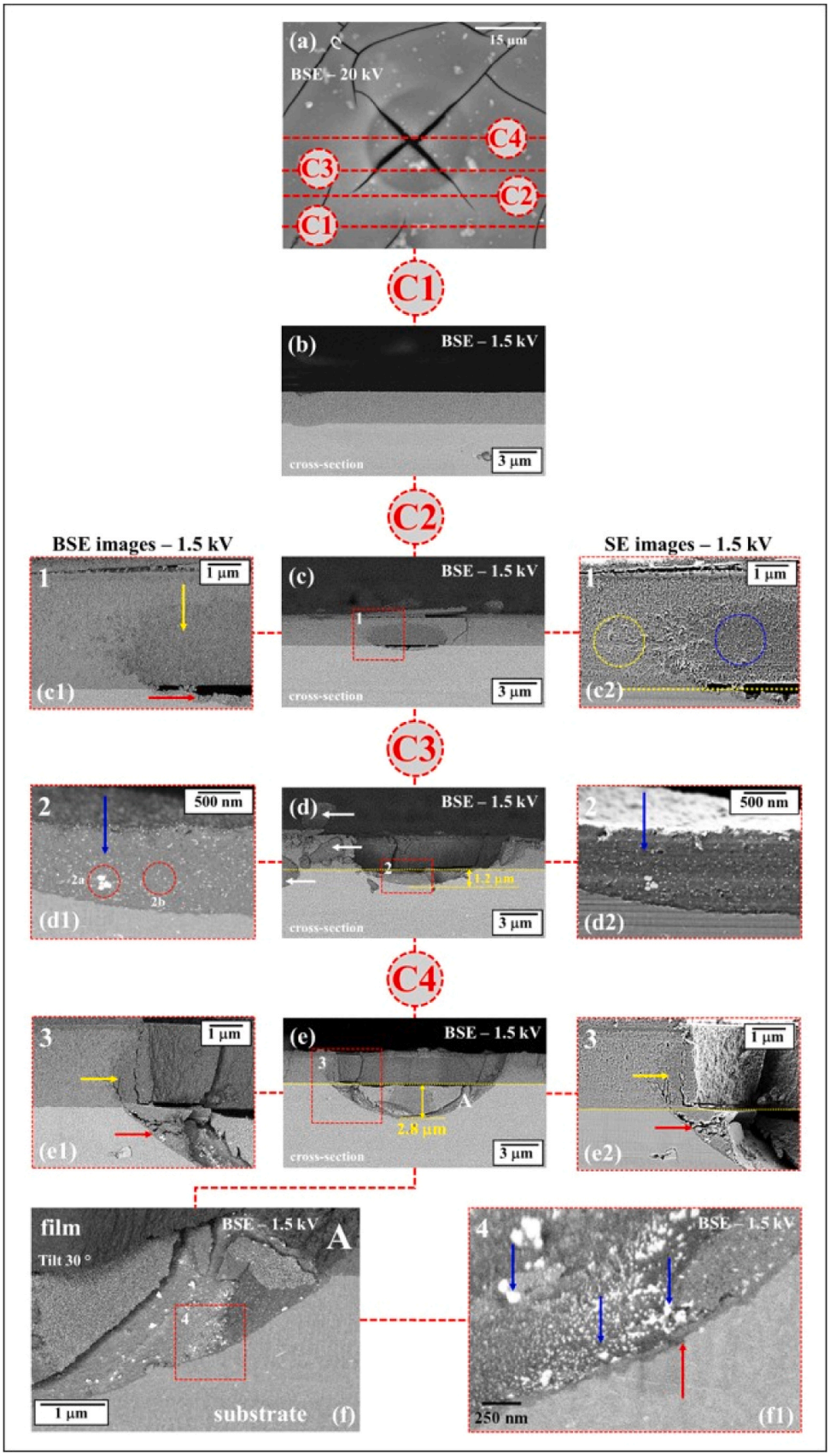

Fig. 12. Scanning electron micrographs of the surface of anodized aluminium alloy after immersion in 0.1 mol L^{-1} NaCl solution for 24 h: (a) pit in AA2198-T8 alloy; (b–e) cross-sectional views of the pit, showing ultramicrotomy cuts C1–C4; (c1–d1) and (c2–d2) are higher magnifications of dashed squares in (c–e) in BSE and SE modes, respectively; (f) and (f1) show higher magnifications of region A in (e). Red dashed lines in (a) mark cut locations, with yellow arrows highlighting modified film, blue arrows indicating copper redeposition, and circles distinguishing modified and unmodified film. Yellow dashed lines mark the film/alloy interface.

(c)), as the cut advances toward the centre of the pit. Fig. 12 (d1) and (d2) show a magnified view of the dashed region 2 in Fig. 12 (d), where a corrosion product can be observed on the pit wall, with an approximate thickness of 1 μm, as indicated by the blue arrows.

The bright spots visible in both images (Fig. 12 (d1) and (d2)) may indicate the presence of copper nanoparticles. Several hypotheses can be proposed to explain the origin of these nanoparticles, which are linked to substrate degradation and the formation of corrosion products. Literature on the anodizing of copper-containing alloys highlights that copper enrichment occurs at the film/alloy interface during the anodizing process [127–132]. This enrichment is followed by the coalescence of copper in solid solution, leading to the formation of nanoparticles at this interface [133]. As the corrosive process advances, these copper nanoparticles may protrude into the corrosion product at the film/alloy interface.

Copper, owing to its intrinsic properties, can exacerbate the corrosion process by acting as nanocathodes, promoting local electrochemical reactions within the corroding cavities. Dissolved copper from the alloy matrix can redeposit onto these nanoparticles, contributing to the growth of the agglomerates. This explanation is supported by observations in the regions marked by the red dashed circles 2a and 2b in Fig. 12 (d1). In these regions, the size of copper particle agglomerates is approximately 80 nm in region 2a and about 5 nm in region 2b. The difference in size may be attributed to the process of copper redeposition in region 2b, as literature suggests that the initial agglomerates formed during anodizing typically measure around 5 nm [133].

Another aspect to note is that the presence of copper nanoparticles within the pits which explains the copper signal detected by the EDX maps in regions associated with these sites (Fig. 4). The elevated copper signal in these areas is due to the increased interaction between the incident electrons, originating from the electron beam, and the copper nanoparticles within the pit.

Fig. 12 (e) shows the final cut, C4, which corresponds to the centre of the localized attack. A circular cavity is observed below the film/alloy interface, with a depth of approximately 2.8 μm, greater than the measurements from cuts C2 and C3 (Fig. 12 (c, d)), due to the fact that cut C4 was made at the center of the pit.

Fig. 12 (e1) and (e2) show a magnified view of the dashed region 3 in Fig. 12 (e), where the corroded substrate (indicated by the blue arrow) can be observed, along with the presence of the modified anodic film (as reported in Fig. 11 (c-c2)) at the edges of the cavity (indicated by the yellow arrows). This suggests that the modified film extends across the entire area above the cavity, confirming surface observations of the pits, which displayed a darker coloration compared to the adjacent oxide, as reported in Figs. 6 and 7.

Fig. 12 (f) shows a magnified view of region A (tilted at 30º), indicated in Fig. 12 (e), where the corroded region and bright spots (associated with copper redeposition) can be observed. Higher magnification of the highlighted region 4 is presented in Fig. 12 (f1), detailing the corroded substrate (indicated by the red arrow), and the presence of copper nanoparticles in the corroded region (indicated by the blue arrows). It is noted that corrosion products were found only at the edge of the cavity (Fig. 12 (e1)), while the central region was free of these products, likely due to detachment during the ultramicrotomy cutting process.

The results presented in this section suggest that the initiation of localized corrosion in the anodized alloy is closely associated to the location of defects within the anodic film. Specifically, defects at the film/alloy interface are more likely to cause localized corrosion, in line with those noted in an Al-Cu-Li alloys under similar anodizing conditions [29,36]. The results challenge previous assumptions that surface defects dictate the onset of corrosion, suggesting instead that the integrity of the anodic film and the underlying substrate plays a critical role. The differences in contrast and morphology indicate that corrosion products significantly alter the structure of the anodic film, leading to localized degradation.

Moreover, Fig. 13 reveals that no evidence of corrosion in the substrate was found in regions where cavities formed on the film surface, reinforcing the observation that defects in the film/alloy interface are crucial in the initiation of localized corrosion.

Fig. 13 (a-d) present scanning electron micrographs of the anodized alloy surfaces after immersion in NaCl solution, highlighting at higher magnification the pits (dashed squares 2, 4, 6, and 8) and the surface defects (dashed squares 1, 3, 5, and 7). These surface defects in the oxides are attributed to the dissolution of high-copper-containing IMPs during the anodizing process, as reported in Fig. 1. The white arrows indicate the presence of a modified anodic film around these corroded areas (as reported in Fig. 12).

Defects at the film/alloy interface are responsible for initiating corrosion in anodized alloys, particularly those caused by the dissolution of high-copper-containing IMPs. The cross-sectional analysis of the defects identified in the dashed squares (1, 3, 5, and 7), corresponding to cuts C1-C4, is presented in Fig. 13 (a1-d2). The cross-sectional images, obtained in both BSE and SE modes, are displayed in Fig. 13 (a1-d1) and (a2-d2), respectively. Based on these images, no evidence of corrosion was observed in the alloy substrate, which is consistent with the surface analysis shown in Fig. 5. These findings highlight the critical role that defects at the film/alloy interface caused by the dissolution of high-copper-containing IMPs play in the development of corrosion in the studied alloys.

It is important to note that the results presented so far have only highlighted corrosion sites caused by defects formed due to the dissolution of high-copper-containing IMPs during the anodizing process. However, in the case of the AA2024-T3 alloy, the pits were also associated with the partial dissolution of IMPs, as shown in Fig. 14.

Fig. 14 (a) presents a scanning electron micrograph of the surface of the AA2024-T3 alloy after immersion, highlighting a site of localized corrosion. The yellow arrow indicates the presence of a modified anodic film surrounding the pit, suggesting localized attack beneath the film (as previously reported in Fig. 12). Fig. 14 (a1) shows the cross-sectional view corresponding to cut C1, where no evidence of corrosion is observed in the alloy substrate. However, in cut C2 (Fig. 14 (b)), a discontinuity in the anodic film extending beneath the anodic film is evident.

The dashed squares 1 and 2 are presented at higher magnification in Fig. 14 (b1) and (c1, c2), respectively. The presence of IMPs is indicated by the red arrows in Fig. 14 (b1), and the EDX analysis in Fig. 14 (b2) confirms that these IMPs consist of Al-Cu-Fe-Mn-Si, as previously reported for this alloy in Fig. 1. The white arrows in Fig. 14 (c) and (c1), obtained in both BSE and SE modes, indicate evidence of corrosion in the alloy substrate.

The results suggest that the diminished corrosion resistance of the anodic films in this alloy is primarily related to the presence of Fe- and Mn-containing particles, which do not contribute to the formation of a protective barrier layer. However, Si-containing particles may also influence the film properties. Two hypotheses can be considered: first, the anodic oxide extending beneath the film (as indicated in Fig. 14 (b)) suggests that the IMP was significantly larger than the final film thickness, causing it to oxidize more rapidly during the initial stage of anodizing once it contacts the anodizing electrolyte, leading to discontinuities in the film. Second, previous studies [30,116,134] on the anodizing behaviour of the AA2024-T3 alloy have demonstrated that Si-containing particles are non-homogeneous, meaning their elemental distribution is uneven. This could explain why part of the IMP oxidized while another part remained intact, leaving remnants of the particle (as indicated by the red arrows in Fig. 14 (b1)). Additionally, silicon exhibits different anodizing behaviour compared to the other elements present in the particle, as it has more positive Gibbs free energies than aluminium, indicating that its oxides are less stable [5].

Failures in the anodic film above second-phase regions containing Si may be exacerbated by localized stresses arising from oxide growth in a confined volume, as well as differences in the Pilling-Bedworth ratio

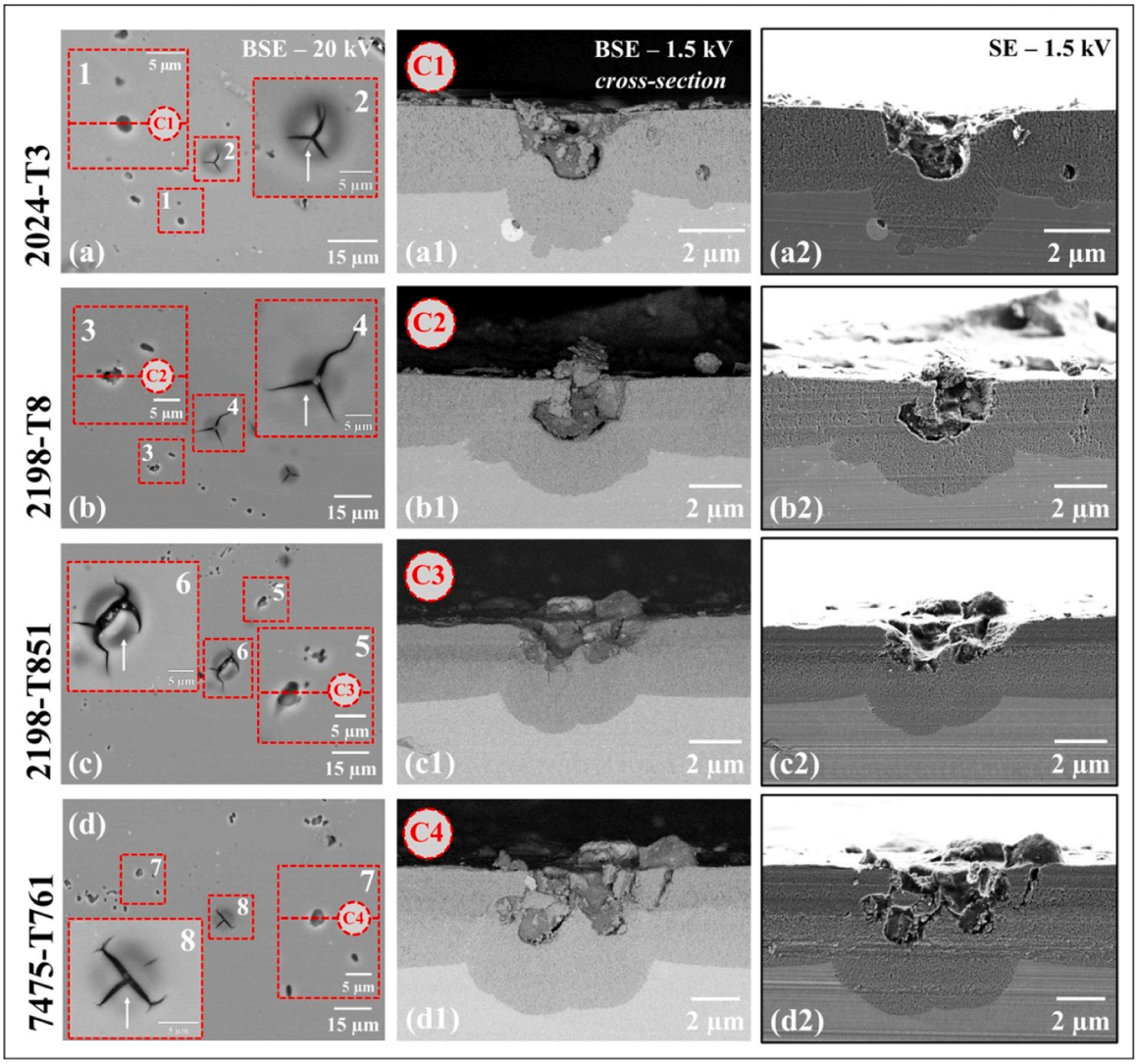

Fig. 13. Scanning electron micrographs of aluminium alloys after anodizing after immersion in 0.1 mol L^{-1} NaCl solution for 24 h: (a–d) show the surfaces at lower magnification; (a1–d2) present cross-sectional images of cuts C1–C4 indicated in the dashed squares (1, 3, 5, and 7) in (a–d). The dashed frames in (a–d) highlight areas of higher magnification, revealing surface defects caused by the dissolution of IMPs during the anodizing process, as well as circular cracks in the anodic film. White arrows in (a–d) indicate the modified anodic film. Images (a–d) were obtained in backscattered electron (BSE) mode at an accelerating voltage of 20 kV, while images (a1–d2) were acquired in both BSE and secondary electron (SE) modes at an accelerating voltage of 1.5 kV.

between the oxides formed [5,135,136]. These failures can serve as preferential sites for corrosion initiation, thereby decreasing the protection provided by the anodic film, as observed in Fig. 14 (a).

The results shown in Fig. 14 suggest that the size and composition of the IMPs must be considered when evaluating defect formation and its impact on the corrosion resistance of anodized aluminium alloys, particularly in alloys such as AA2024-T3, which contain various types of IMPs. In contrast to the other alloys studied, the AA7475-T761, which contains low-copper-containing particles, showed no evidence of pit formation associated with these particles. Fig. 15 presents scanning electron micrographs of a cross-sectional view of the AA7475-T761 alloy after immersion testing, showing a corrosion-free region containing low-copper-containing IMP at the film/alloy interface.

Fig. 15 (a) presents an image of the AA7475-T761 alloy surface after immersion test. Fig. 15 (a1) shows the cross-sectional view corresponding to cut C1, revealing an IMP projected into the anodic film. Fig. 15 (a2) provides a magnified view of region A, highlighted in Fig. 15 (a1), displaying a detailed look at the IMP at the film/alloy interface. The EDX analysis, Fig. 15 (a3), confirms that this IMP has a low copper content (~6.3 wt% Cu), as demonstrated in a previous study by our research group [113], reinforcing the presence of this type of particle in the AA7475-T761 alloy. Fig. 15 (a4) and (a5), which correspond to further magnifications of region 1 in Fig. 15 (a2), obtained in BSE and SE modes, respectively, show no evidence of corrosion, either in the alloy substrate or within the IMP.

These results are consistent with previous studies on the AA2099 alloy [36], which demonstrated that low-copper-containing particles do not significantly impact the corrosion resistance of anodized alloys. As reported in Fig. 1, these particles exhibit a lower anodizing rate compared to the aluminium matrix, resulting in their partial oxidation during the anodizing process. This leads to the incorporation of these particles into the anodic film. Although this partial oxidation may result in thinner regions within the film [117] the study indicates that these areas do not serve as preferential sites for corrosion initiation. To further explore this behaviour, Fig. 15 (a6) and (a7) provide higher magnification views of regions B and C indicated in Fig. 15 (a4) and (a5), respectively. The white arrows in Fig. 15 (a6) and (a7) highlight the interface between low copper-containing IMPs and the anodic film. Based on these observations, it is believed that a barrier layer may be present at this interface, which could play a role in preventing corrosion

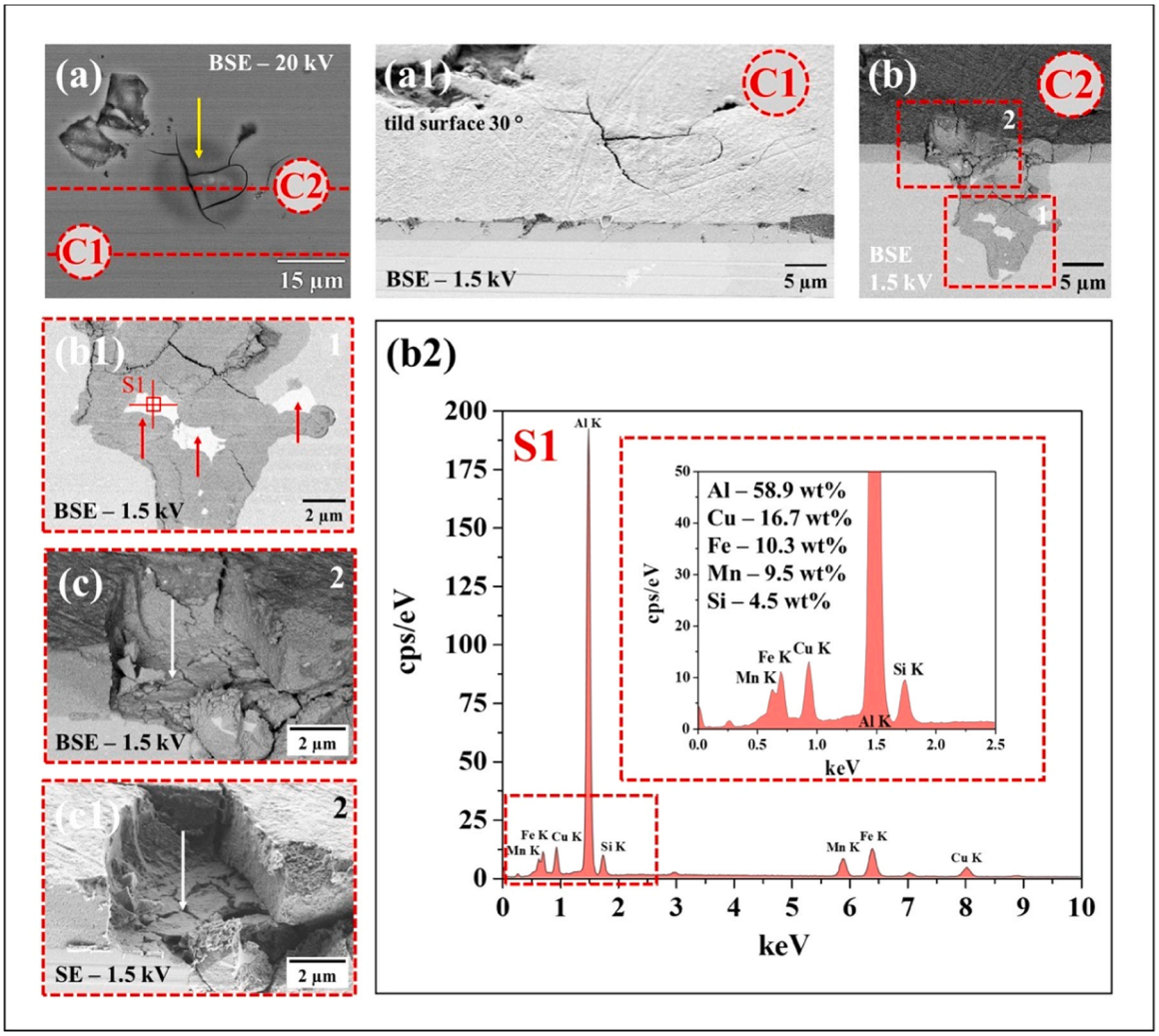

Fig. 14. Scanning electron micrographs of the AA2024-T3 alloy after anodizing after immersion in 0.1 mol L^{-1} NaCl solution for 24 h: (a) lower magnification image of a region associated with a pit; (a1) cross-sectional image of the area corresponding to cut C1, as indicated in (a); (b) cross-sectional image corresponding to cut C2, as indicated in (a); (b1) higher magnification image of the dashed square in (b); (b2) EDX spectrum corresponding to point S1 indicated in (b1); (c, c1) higher magnification images of the dashed square in (b). Red and white arrows in (b1, c, c1) indicate intermetallic particles containing Si and the corroded substrate, respectively. The yellow arrow in (a) highlights the modified anodic film surrounding the crack. Image (a) was obtained in backscattered electron (BSE) mode at an accelerating voltage of 20 kV, while images (a1–c) were acquired in both BSE and secondary electron (SE) modes at an accelerating voltage of 1.5 kV.

initiation.

A comprehensive understanding of both the composition and distribution of IMPs is crucial to optimizing the performance of anodized alloys. The high-copper-containing IMPs play a critical role in the initiation of corrosion in anodized aluminium alloys. In contrast, the absence of significant corrosion around low-copper-containing IMPs in the AA7475-T761 alloy suggests that variations in copper-containing IMPs, as well as the size of the particles, are crucial factors in determining the corrosion resistance of anodized aluminium alloys. Additionally, the presence of silicon in high-copper-containing IMPs, particularly in the AA2024 alloy, must also be considered, as it can further influence the anodizing behaviour and subsequent corrosion resistance.

4. Discussion

The microstructure of the aluminium alloys is crucial in determining both the formation of anodic films and the subsequent corrosion resistance of the anodized alloys. Based on the observation above, a corrosion hierarchy for the anodized alloys investigated has been established, as illustrated in Fig. 16.

The increased density of IMPs not only leads to a decrease in the quality of the anodic film but also significantly raises the number of corrosion-prone sites, depending on their location relative to the film. An increase in IMP density directly correlates with a higher number of defects in the anodic film, which consequently leads to a greater number of corrosion sites, as indicated by the arrows in Fig. 16.

Our previous study [113] demonstrated that the AA2024-T3 alloy has the highest IMP density, with 3472 ± 157 particles/mm^2, as well as the second-largest average particle size of 3.9 ± 2.6 µm, and the highest surface area coverage of 1.4 %. The AA2198 alloys, in both T8 and T851 tempers, exhibit intermediate values, with the T8 condition having a higher density (1948 ± 242 particles/mm^2) compared to T851 (1389 ± 149 particles/mm^2), while both conditions show similar average particle sizes and surface coverage. Finally, the AA7475-T761 alloy has the lowest particle density, with 626 ± 75 particles/mm^2, the smallest average particle size of 3.7 ± 2.94 µm, and the lowest surface coverage of 0.14 %. These findings indicate that alloys with a higher density of IMPs, such as AA2024-T3, exhibit a greater likelihood of pit formation due to the increased number of defects, resulting in more corrosion sites when exposed to an aggressive environment (Fig. 3).

The triangular diagram in Fig.17 further illustrates the influence of

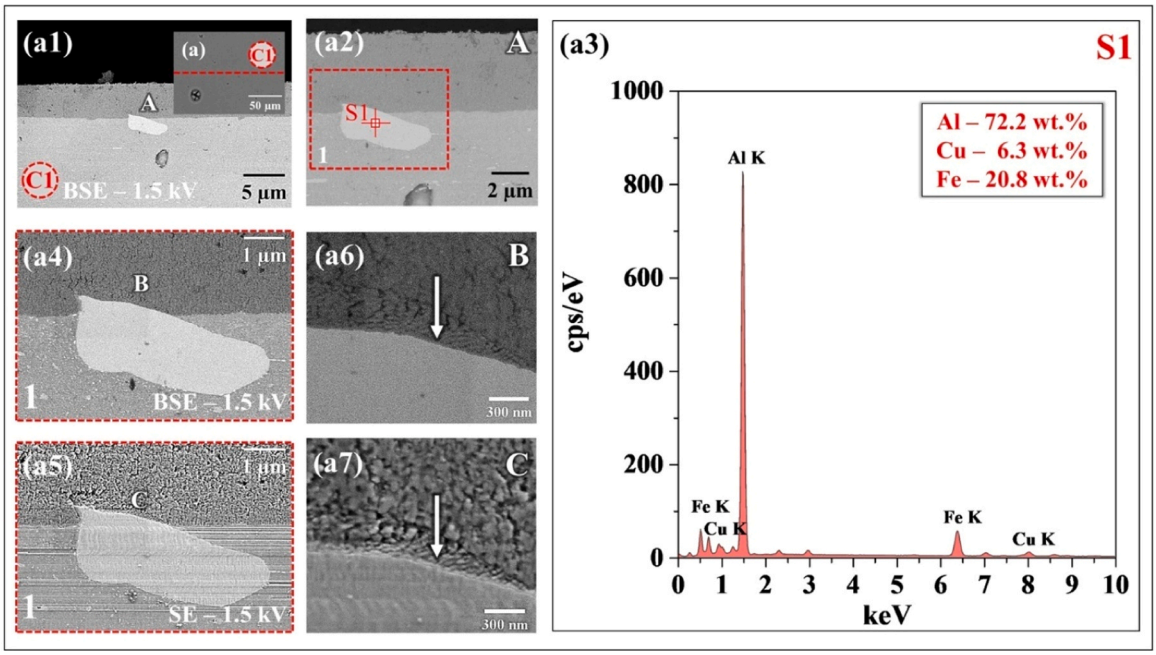

Fig. 15. Scanning electron micrographs of the anodized AA7475-T761 aluminium after immersion in 0.1 mol L^{-1} NaCl solution for 24 h: (a) surface image; (a1) cross-sectional image corresponding to cut C1 indicated in (a); (a2) higher magnification of region A indicated in (a1); (a3) EDX spectrum corresponding to point S1 in (a2); (a4, a5) higher magnification of the dashed regions in (a2); (a6, a7) higher magnification views of regions B and C indicated in (a4) and (a5), respectively. The white arrows in (a6) and (a7) indicate the interface between low copper-containing intermetallic particles (IMPs) and the anodic film. Image (a) was obtained in backscattered electron (BSE) mode at an accelerating voltage of 20 kV, while images (a1, a2, and a4-a7) were acquired in both BSE and secondary electron (SE) modes at an accelerating voltage of 1.5 kV.

IMP chemical composition and location on the corrosion resistance of anodized alloys, highlighting that high-copper-containing IMPs are more detrimental than silicon-containing ones. Although Si-containing IMPs in the AA2024-T3 alloy can also generate discontinuities at the film/alloy interface depending on their location, our study demonstrated that high-copper-containing IMPs have a more significant impact on reducing the corrosion resistance of the alloys (Fig. 4).

The relationship between the chemical composition, location of IMPs, and corrosion susceptibility of anodized alloys is crucial. IMPs situated at the film/alloy interface are more likely to cause localized corrosion (Fig. 6), whereas those within the film or on the surface have minimal or no detrimental effect (Figs. 4 and 11). The dissolution of high-copper-containing IMPs creates micrometric defects that serve as preferential sites for corrosion initiation (Fig. 12). These defects facilitate electrolyte penetration and exposure of the substrate, accelerating the onset of localized corrosion. This trend correlates with the number of IMPs, with AA2024-T3 being the most affected, followed by the Al-Cu-Li alloys (AA2198) and, to a lesser extent, the Al-Zn-Mg alloy (AA7475-T761).

As indicated in Fig. 16, there is a clear sequence for the development of pits in anodized alloys. Up to 24 h, corrosion manifests predominantly as circular pits (Figs. 6 and 8). After 48 h, a transition phase is observed, which varies across different alloys. Notably, only the AA7475-T761 alloy exhibited intergranular corrosion (IGC) at this stage (Fig. 8). Finally, after 60 h, pit morphology evolves into irregular pits, characterized by the presence of IGC and crystallographic corrosion due to local chemical changes (Fig. 9). This suggests that prolonged exposure to aggressive environments promotes pit evolution from uniform, shallow features to more complex morphologies involving intergranular attack and crystallographic propagation mechanisms. This evolution strongly depends on the historical processing characteristics of each alloy and its microstructural features [137–140], which influence the susceptibility to localized corrosion and the overall material deterioration process [141–143].

When evaluating the corrosion resistance of anodic films, the barrier film serves as the primary protective component, acting as a uniform shield that prevents contact between the substrate and corrosive environments [144]. In contrast, the porous film, while not directly contributing to corrosion resistance, plays an important role in applications such as enhancement of coating adhesion or sealing [145]. Corrosion protection, therefore, largely depends on the integrity of the barrier layer. Studies on anodizing of the AA2050 alloy, conducted under the same anodizing parameters used in this work, demonstrated that, although increasing anodizing time results in a thicker porous film, it does not substantially improve corrosion resistance [29]. The presence of defects at the film/alloy interface, particularly those caused by dissolution of high-copper-containing IMPs, is the most critical factor. This finding is consistent with the behaviour observed for the AA7475-T761 alloy, with the thickest anodic film compared to the other alloys (as reported in Fig. 2), and superior corrosion resistance (Fig. 3). The determining factor was the lowest density of high-copper-content IMPs, resulting in fewer critical defects in the barrier layer. In contrast, alloys such as AA2024-T3 and AA2198, which have a higher density of these IMPs, are more susceptible to corrosion due to the increased number of defects at the film/alloy interface.

Another relevant aspect to consider is the presence of low-copper-containing IMPs in the AA7475-T761 alloy. Even when located at the film/alloy interface (Fig. 15), these particles did not negatively affect corrosion resistance. Although these particles exhibit a lower anodizing rate (as reported in Fig. 2), the oxides formed on them can be relatively stable, contributing to the integrity of the surrounding film. These stable oxides may compensate for the reduced film thickness in these regions, thus preventing localized corrosion. This phenomenon was also observed for the AA2099 alloy, under anodizing conditions similar to those in this work, where the authors suggested that transforming high-copper-containing IMPs into low-copper-content ones could enhance the corrosion resistance of anodized alloys [36]. Eliminating or minimizing high-copper-content particles would be the most effective strategy to prevent the formation of cavities and, consequently, improve the corrosion resistance of the anodic film without the need for additional

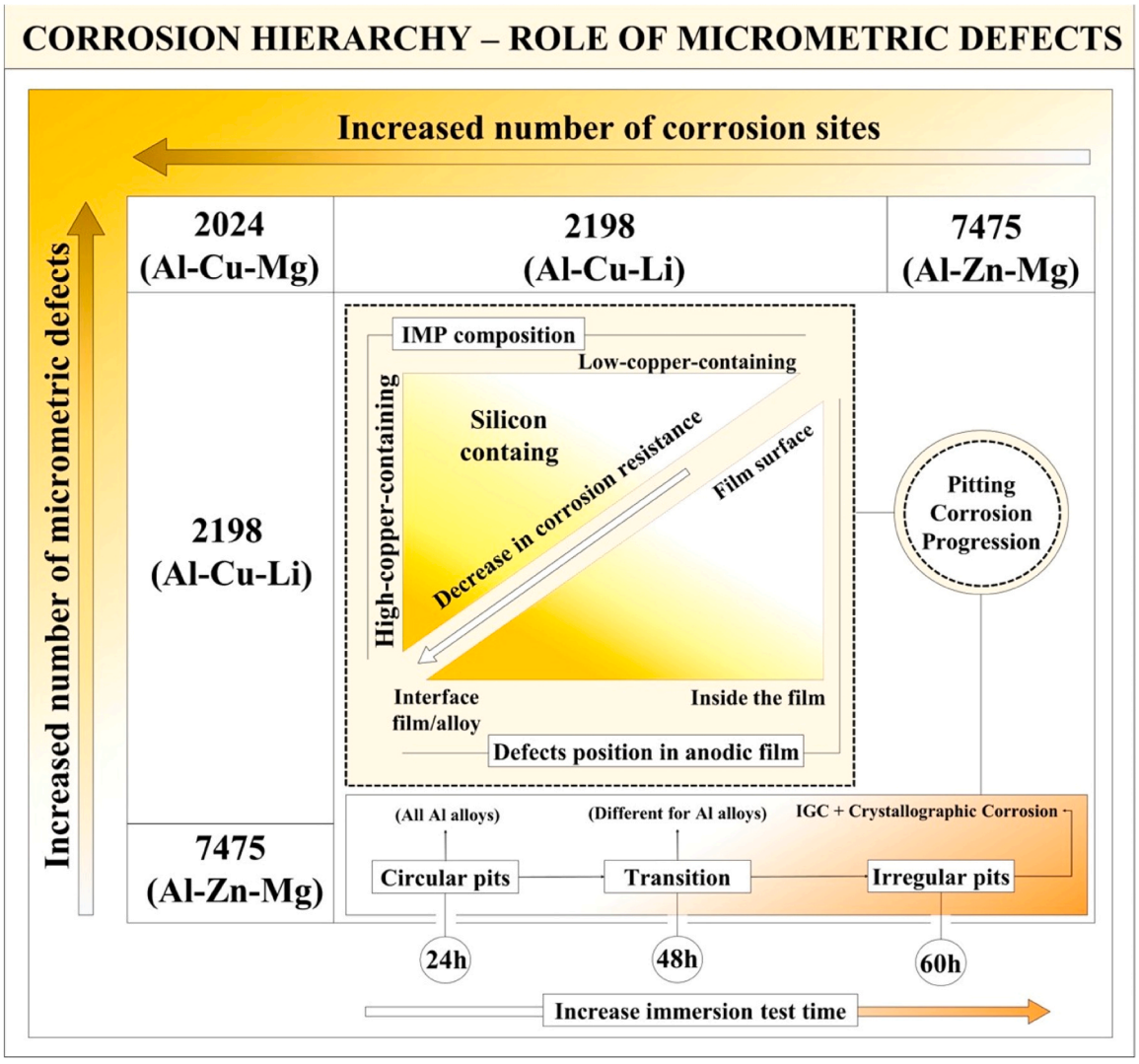

Fig. 16. Corrosion hierarchy for the anodized aluminium alloys tested in this study, based on the results reported.

treatments, such as sealing. However, while the transformation from high-copper-content to low-copper-containing IMPs has been mentioned as a possibility, the study did not provide details on the methods to achieve this transformation. For practical application, it is crucial to investigate the feasibility and effectiveness of these methods under real production conditions, considering the full processing history of the alloy. Such an approach would be particularly advantageous for alloys like AA2198, which contain only one type of IMP. Up to now, no studies in the literature have addressed methods for transforming high-copper-content (> 12 wt% Cu) IMPs into low-copper-content (< 7 wt% Cu) ones.

Based on the findings of this study, along with information from the literature [8], it is evident that high-copper-containing IMPs play a critical role in reducing the corrosion resistance of anodic films. The formation of defects and discontinuities associated with the dissolution of these IMPs during the anodizing process significantly decreases the protective properties of the anodic film. As a result of these findings, a comprehensive corrosion mechanism is proposed that considers the micrometric defects induced by high-copper-containing IMPs. This mechanism traces the origin of these defects to the development of localized corrosion in aluminium alloys, highlighting their key characteristics, as illustrated in Fig. 17.

The surface preparation for anodizing (mechanical grinding followed by polishing with diamond suspension) reveals the presence of constituent intermetallic particles (IMPs) in the aluminium alloy, which appear as bright spots due to the high atomic numbers of the elements they contain (stage 1), as addressed in Fig. 1.

At higher magnification, the dashed region (C1) from stage 1 provides a cross-sectional view, showing an IMP on the surface, and a second one just below the surface within the alloy. An air-formed film is also observed, interrupted by the surface IMP (stage 2).

In stage 3, a cross-sectional view of the region during anodizing in the TSA solution is analysed. The anodic oxidation process involves ion migration through a thin anodic film under the influence of an electric field. Approximately 40 % of the film thickness forms at the film/electrolyte interface, with the remaining 60 % generated at the metal/film interface (as indicated by the red dashed square) [147]. Due to high concentrations of Cu, Fe, Mg, Mn, and Li, IMPs in contact with the anodizing electrolyte oxidize more rapidly than the aluminium matrix or form highly soluble oxides. This process results in cavities (defects) on both the surface (a) and at the film/alloy interface (b), ultimately leading to a non-uniform anodic film thickness (stage 4).

Surface cavities do not significantly contribute to localized corrosion initiation (Fig. 13), as the underlying barrier layer beneath these cavities remains compact, similar to the barrier layer formed by the alloy matrix. However, if an IMP fully dissolves, the barrier layer develops defects, causing discontinuities in the anodic film. These defective regions at the film/alloy interface become vulnerable to localized corrosion initiation,

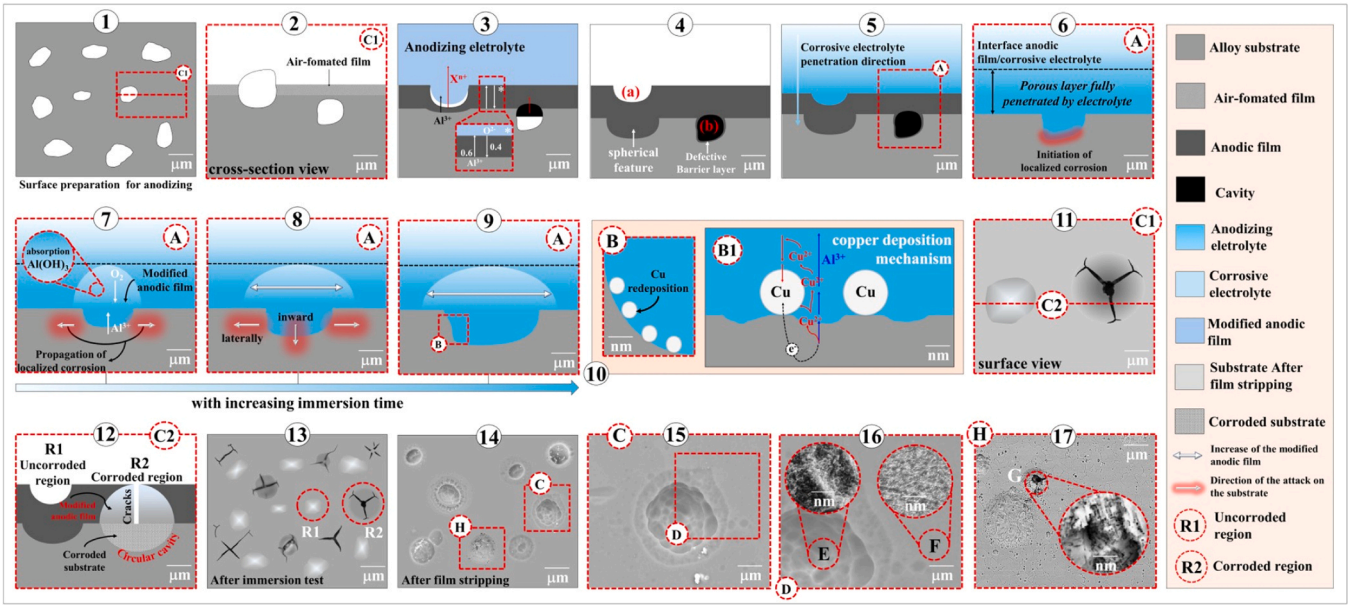

Fig. 17. Schematic diagrams illustrating defect formation during anodizing and its influence on localized corrosion in aluminium alloys exposed to a corrosive electrolyte. The diagrams show: (1) a polished alloy surface with high-copper-containing IMPs; (2) a cross-sectional view of the dashed region in (1), corresponding to cut C1; (3) the anodizing process, highlighting intermetallic dissolution on the surface and below the alloy matrix; (4) the final cross-sectional view after anodizing, showing defects at the surface and the film/alloy interface; (5) penetration of the corrosive electrolyte through the anodic film; (6) a higher magnification of the dashed region in (5), illustrating localized corrosion initiation at the defect site on the film/alloy interface; (7–9) corrosion propagation in all directions, affecting both lateral and depth profiles of the anodic film and leading to crack formation and progression; (10) copper nanoparticle redeposition as a result of Cu ions in the electrolyte near the exposed alloy; (11) a surface view of the anodic film after immersion testing, corresponding to the dashed region in (1); (12) a cross-sectional view corresponding to cut C2 in (11); (13–17) characteristics of corrosion sites and surface analysis after immersion testing and film stripping. This mechanism is supported by both our findings and existing literature [8,29–31,33,36,116,117,146].

allowing direct contact between the substrate and the corrosive environment. This process is shown in stage 6, which provides a magnified view of the dashed region (A) from stage 5.

The progression of localized corrosion at the film/alloy interface is demonstrated, with corrosion products diffusing through anodic film pores, leading to structural modification (stage 7). As the corrosive process advances (stages 8 and 9), the modified anodic film forms a solid spherical structure that appears elliptical on the surface (Fig. 6) and semi-elliptical in cross-section (Fig. 12). Over time, the accumulation of corrosion products causes volumetric expansion stress, resulting in cracks that allow the corrosive environment to reach the substrate.

Local electrochemical processes within the cavities can lead to copper (Cu) nanoparticle deposition on their walls (Fig. 12 (d-d2)), illustrated in dashed square B in stage 9, and further enlarged in stage 10. As shown schematically in stage B1 and in the literature [146], aluminium oxidation at anodic sites releases Al^{3+} and Cu^{2+} ions. When Cu^{2+} concentration reaches a critical level, these ions reduce and deposit as metallic copper at cathodic sites. During this process, electrons from aluminium oxidation move to the cathodic sites, where they reduce Cu^{2+} ions, completing the circuit leading to copper redeposition. Cu redeposition is intensified at the film/alloy interface in Cu-rich regions formed during anodizing, which act as nanocathodes, further promoting copper redeposition from the matrix during corrosion [131].

After immersion test, a corrosion site as pit, with circular morphology, is observed, surrounded by a modified anodic film and cracks from oxide dehydration in this area during drying. This feature is located in a previously defect-free region on the oxide surface (Fig. 6), illustrated in stage 11, where a magnified view of the red dashed square in stage 1 is shown after immersion testing.

In stage 12, a higher magnification of the dashed region (C2) in stage 11 provides a cross-sectional analysis of the surface defect (R1 - uncorroded) and localized attack (R2 - corroded) areas. Corrosion is observed only in regions associated with defects at the film/alloy interface (Fig. 12), with no substrate attack beneath the surface defect (Fig. 13).

At lower magnification, the surface of the anodized sample post-immersion test is shown (stage 13), revealing corroded sites and cracks surrounded by a modified anodic film. Dashed circles R1 and R2 indicate the region shown in stage 11, highlighting both uncorroded and corroded areas. After film removal (stage 14), the pit morphology and extent become evident, and at higher magnification (dashed square C), the circular shape of the pit is observed (stage 15). In dashed square D, a high magnification analysis of the corroded (dashed circle E) and uncorroded (dashed circle F) regions reveals a porous substrate in the corroded areas, while intact regions display a scalloped surface (Fig. 8), as presented in stage 16.

Stage 17 presents a higher magnification of the dashed region H in stage 14, showing crystallographic corrosion within the cavity (dashed circle G). Considering the microstructural characteristics of the alloys, these cavities formed during prolonged immersion serve as preferential sites for corrosion propagation, including crystallographic corrosion (Fig. 9), which is strongly influenced by the thermomechanical history of the alloy [137,148]. As a result, the effectiveness and long-term durability of the anodic films under service conditions are deteriorated.

One aspect not addressed in the schematic diagram presented in Fig. 17 is the size of the IMPs. Observations indicate that IMPs exceeding the anodic film thickness can directly expose the alloy substrate. This phenomenon is particularly observed in the AA2024-T3 alloy (Fig. 14) but is also relevant to other alloy systems. In this context, IMP size is a critical parameter to consider for each alloy type, as particle characteristics vary significantly across aluminium alloys depending on processing conditions and thermomechanical treatments [137,149].

Research on corrosion mechanisms in anodized aluminum alloys indicates that traditional analysis methods may not capture the full complexity of the phenomenon. Currently, no studies have investigated the corrosion resistance of these alloys in a three-dimensional perspective. While some studies have used 3D reconstructions to analyse micrometric-scale defect formation [36] this technique has rarely been

applied to corrosion sites, focusing instead on uncoated alloys [150–153]. Most analyses, including those in this study, are limited to two-dimensional observations, which may not fully reveal the complexities inherent to corrosion processes. In this context, adopting three-dimensional volumetric reconstructions could provide significant advantages, offering deeper insights into the initiation and propagation of corrosion and enhancing the development of aluminium alloys with improved corrosion resistance.

5. Conclusions

a) The corrosion resistance of anodized aluminium alloys studied in the present work, including AA2024-T3, AA2198-T8, AA2198-T851, and AA7475-T761, is largely influenced by the population, composition and size of constituent intermetallic particles in the alloys.
b) In all alloys, localized corrosion initiates at defects formed at the film/alloy interface due to the dissolution of high-copper-containing particles (> 12 wt% Cu) during anodizing. These defects compromise the integrity of the protective barrier film, exposing the underlying substrate alloy to corrosive environment, enabling corrosion initiation. Further, cavity defects located at the film surface or within the anodic film but away from the film/alloy interface, do not act as corrosion initiation sites.
c) During prolonged exposure, corrosion propagates from the initiation sites inward and laterally under anodic films, resulting in localized corrosion in the forms of crystallographic dissolution or intergranular corrosion, which appear as circular corrosion features on anodic film surface. The corrosion propagation mechanism and rate are independent of the anodic film resistance but determined by the microstructure of bulk alloys.
d) In the AA2024-T3 alloy, corrosion initiation occurs not only at cavity defects formed from the dissolution of high-copper-containing particles located at the film/alloy interface, but also at partially dissolved Si-containing particles located at the film/alloy interface, which expose the alloy substrate to corrosive environment.
e) In the AA7475-T761 alloy, low-copper-containing particles (< 7 wt % Cu) do not significantly compromise the corrosion resistance of the anodized alloy, indicating that the barrier layer formed over these low-copper-containing particles is sufficiently compact to protect the underlying alloy.

CRediT authorship contribution statement

Zhou Xiaorong: Writing – review & editing, Visualization, Supervision, Resources, Funding acquisition. **Costa Isolda:** Writing – review & editing, Supervision, Resources. **Chen Jinghui:** Investigation. **Araujo João Victor:** Writing – original draft, Visualization, Supervision, Investigation, Data curation, Conceptualization.

Declaration of Competing Interest

The authors declare that they have no known competing financial interests or personal relationships that could have appeared to influence the work reported in this paper.

Acknowledgements

The authors gratefully acknowledge the financial support provided by FAPESP under grant numbers 2019/18388-1 and 2022/06935-0, awarded for the Ph.D. studies of João Victor de Sousa Araujo. Additionally, this work was supported by the Engineering & Physical Sciences Research Council (EPSRC) under grant EP/S004963/1.

Data availability

Data will be made available on request.

References

[1] J.M. Runge, The Metallurgy of Anodizing Aluminum, Springer International Publishing, Cham, 2018, https://doi.org/10.1007/978-3-319-72177-4.
[2] G.E. Thompson, G.C. Wood, Anodic Films on Aluminium, in: Corrosion: Aqueous Processes and Passive Films, Academic Press INC. (LONDON) LTD, 1983, pp. 205–329, https://doi.org/10.1016/B978-0-12-633670-2.50010-3.
[3] G.E. Thompson, H. Habazaki, K. Shimizu, M. Sakairi, G.C. Wood, Anodizing of aluminium alloys, Aircr. Eng. Aerosp. Technol. 71 (1999) 228–238.
[4] G.E. Thompson, P. Skeldon, X. Zhou, K. Shimizu, H. Habazaki, C.J.E. Smith, Improving the performance of aerospace alloys, Aircr. Eng. Aerosp. Technol. 75 (2003) 372–379, https://doi.org/10.1108/00022660310484301.
[5] H. Habazaki, K. Shimizu, P. Skeldon, G.E. Thompson, G.C. Wood, X. Zhou, Effects of alloying elements in anodizing of aluminium, Trans. Inst. Met. Finish 75 (1997) 18–23, https://doi.org/10.1080/00202967.1997.11871137.
[6] Y. Ma, X. Zhou, J. Wang, G.E. Thompson, W. Huang, J.O. Nilsson, M. Gustavsson, A. Crispin, Discoloration of anodized AA6063 aluminum alloy, J. Electrochem. Soc. 161 (2014), https://doi.org/10.1149/2.065406jes.
[7] Y. Ma, X. Zhou, K. Li, S. Pawar, Y. Liao, Z. Jin, Z. Wang, H. Wu, Z. Liang, L. Liu, Corrosion and anodizing behavior of T1 (Al_2CuLi) precipitates in Al-Cu-Li alloy, J. Electrochem. Soc. 166 (2019) C296–C303, https://doi.org/10.1149/2.0891912jes.
[8] J.V. de, S. Araujo, M. Milagre, I. Costa, A historical, statistical and electrochemical approach on the effect of microstructure in the anodizing of Al alloys: a review, Crit. Rev. Solid State Mater. Sci. 0 (2023) 1–61, https://doi.org/10.1080/10408436.2023.2230250.
[9] M.P. Martínez-Viademonte, S.T. Abrahami, T. Hack, M. Burchardt, H. Terryn, A review on anodizing of aerospace aluminum alloys for corrosion protection, Coatings 10 (2020) 1106, https://doi.org/10.3390/coatings10111106.
[10] I. Tsangaraki-Kaplanoglou, S. Theohari, T. Dimogerontakis, Y.M. Wang, H. H. Kuo, S. Kia, Effect of alloy types on the anodizing process of aluminum, Surf. Coat. Technol. 200 (2006) 2634–2641, https://doi.org/10.1016/j.surfcoat.2005.07.065.
[11] V.R. Capelossi, M. Poelman, I. Recloux, R.P.B. Hernandez, H.G. de Melo, M. G. Olivier, Corrosion protection of clad 2024 aluminum alloy anodized in tartaric-sulfuric acid bath and protected with hybrid sol–gel coating, Electrochim. Acta 124 (2014) 69–79, https://doi.org/10.1016/j.electacta.2013.09.004.
[12] V.R. Capelossi, M. Poelman, R.P.B. Hernandez, H.G. De Melo, M. Olivier, Corrosion protection of clad AA2024 anodized in sulfuric and tartaric-sulfuric acid sealed with sol-gel hybrid coatings, Surf. Coat. Technol. 200 (2016) 2634–2641.
[13] F.M. Queiroz, A.F.S. Bugarin, N.P. Hammel, V.R. Capelossi, M. Terada, I. Costa, EIS behavior of anodized and primer coated AA2198–T851 compared to AA2024–T3 exposed to salt spray CASS test, Surf. Interface Anal. 48 (2016) 755–766, https://doi.org/10.1002/sia.5982.
[14] O.M. Prada Ramirez, F.M. Queiroz, M. Terada, U. Donatus, I. Costa, M.G. Olivier, H.G. de Melo, EIS investigation of a Ce-based post-treatment step on the corrosion behavior of Alclad AA2024 anodized in TSA, Surf. Interface Anal. (2019) 1–16, https://doi.org/10.1002/sia.6633.
[15] O.M. Prada Ramirez, F.M. Queiroz, M.A. Tunes, R.A. Antunes, C.L. Rodrigues, A. Lanzutti, S. Pogatscher, M.-G. Olivier, H.G. De Melo, Tartaric-sulfuric acid anodized clad AA2024-T3 post-treated in Ce-containing solutions at different temperatures: Corrosion behavior and Ce ion distribution, Appl. Surf. Sci. 534 (2020) 147634, https://doi.org/10.1016/j.apsusc.2020.147634.
[16] H. Costenaro, F.M. Queiroz, M. Terada, M.G. Olivier, I. Costa, H.G. De Melo, Corrosion protection of AA2524-T3 anodized in tartaric-sulfuric acid bath and protected with hybrid sol-gel coating, Key Eng. Mater. 710 (2016) 210–215, https://doi.org/10.4028/www.scientific.net/KEM.710.210.
[17] H. Costenaro, A. Lanzutti, Y. Paint, L. Fedrizzi, M. Terada, H.G. de Melo, M. G. Olivier, Corrosion resistance of 2524 Al alloy anodized in tartaric-sulfuric acid at different voltages and protected with a TEOS-GPTMS hybrid sol-gel coating, Surf. Coat. Technol. 324 (2017) 438–450, https://doi.org/10.1016/j.surfcoat.2017.05.090.
[18] M. Terada, F.M. Queiroz, H. Costenaro, V.H. Ayusso, M. Olivier, I. Costa, H.G. de Melo, Effect of cerium addition to a hydrothermal treatment on the corrosion protection of the tartaric-sulfuric acid anodized AA2524-T3, Corrosion 75 (2019) 1110–1117, https://doi.org/10.5006/3063.
[19] M. Terada, F.M. Queiroz, D.B.S. Aguiar, V.H. Ayusso, H. Costenaro, M.G. Olivier, H.G. de Melo, I. Costa, Corrosion resistance of tartaric-sulfuric acid anodized AA2024-T3 sealed with Ce and protected with hybrid sol–gel coating, Surf. Coat. Technol. 372 (2019) 422–426, https://doi.org/10.1016/j.surfcoat.2019.05.028.
[20] T. Vignoli Machado, P. Atz Dick, G.H. Knörnschild, L.F.P. Dick, The effect of different carboxylic acids on the sulfuric acid anodizing of AA2024, Surf. Coat. Technol. 383 (2020) 125283, https://doi.org/10.1016/j.surfcoat.2019.125283.
[21] P.O. Samaniego-Gámez, F. Almeraya-Calderon, E. Maldonado-Bandala, J. Cabral-Miramontes, D. Nieves-Mendoza, J. Olguin-Coca, L.D. Lopez-Leon, L.G. Silva Vidaurri, P. Zambrano-Robledo, C. Gaona-Tiburcio, Corrosion behavior of AA2055 aluminum-lithium alloys anodized in the presence of sulfuric acid solution, Coatings 11 (2021) 1278, https://doi.org/10.3390/coatings11111278.
[22] X. Yu, G. Zhang, Z. Zhang, Y. Wang, Research on corrosion resistance of anodized and sealed 6061 aluminum alloy in 3.5 % sodium chloride solution, Int. J. Electrochem. Sci. 18 (2023) 100092, https://doi.org/10.1016/j.ijoes.2023.100092.
[23] J. Cabral-Miramontes, F. Almeraya-Calderón, C.T. Méndez-Ramírez, J.P. Flores-De los Rios, E. Maldonado-Bandala, M.Á. Baltazar-Zamora, D. Nieves-Mendoza, M. Lara-Banda, G. Pedraza-Basulto, C. Gaona-Tiburcio, Effect of citric acid hard

anodizing on the mechanical properties and corrosion resistance of different aluminum alloys, Materials 17 (2024) 4285, https://doi.org/10.3390/ma17174285.
[24] R. Fabris, G. Masi, M.C. Bignozzi, Corrosion behavior of aluminum alloys in different alkaline environments: effect of alloying elements and anodization treatments, Coatings 14 (2024) 240, https://doi.org/10.3390/coatings14020240.
[25] R. del Olmo, M. Mohedano, P. Visser, A. Rodriguez, E. Matykina, R. Arrabal, Effect of cerium (IV) on thin sulfuric acid anodizing of 2024-T3 alloy, J. Mater. Res. Technol. 15 (2021) 3240–3254, https://doi.org/10.1016/j.jmrt.2021.09.117.
[26] Y. Ma, X. Zhou, W. Huang, G.E. Thompson, X. Zhang, C. Luo, Z. Sun, Localized corrosion in AA2099-T83 aluminum-lithium alloy: the role of intermetallic particles, Mater. Chem. Phys. 161 (2015) 201–210, https://doi.org/10.1016/j.matchemphys.2015.05.037.
[27] J.S. Pinheiro, C.T. Oliveira, G. Regio, N. Goi, J.Z. Ferreira, Characterization of anodized and bare 7075-T6 aluminum alloy treated with Zr-based conversion coating, Tecnol. Metal. Mater. Min. 18 (2021) e2407, https://doi.org/10.4322/2176-1523.20202407.
[28] J.S. Pinheiro, G. Regio, H.R.P. Cardoso, C.T. Oliveira, J.Z. Ferreira, Influence of concentration and pH of hexafluorozirconic acid on corrosion resistance of anodized AA7075-T6, Mater. Res. 22 (2019) 1–11, https://doi.org/10.1590/1980-5373-mr-2019-0048.
[29] Y. Ma, H. Wu, X. Zhou, K. Li, Y. Liao, Z. Liang, L. Liu, Corrosion behavior of anodized Al-Cu-Li alloy: the role of intermetallic particle-introduced film defects, Corros. Sci. 158 (2019) 108110, https://doi.org/10.1016/j.corsci.2019.108110.
[30] J.V. de Sousa Araujo, M. Xavier Milagre, R. Emil Klumpp, V. Hugo Ayusso, U. Donatus, I. Costa, TSA anodising voltage effects on the near-surface coarse intermetallic particles in the AA2024-T3 and AA2198-T8 alloys, Corros. Eng. Sci. Technol. 57 (2022) 380–396, https://doi.org/10.1080/1478422X.2022.2071666.
[31] J.V. Araujo, M. Xavier Milagre, A.D. Gabbardo, R.E. Klumpp, I. Costa, (Digital Presentation) The effect of tartaric-sulfuric acid (TSA) anodizing on the corrosion resistance of the AA7475-T761, ECS Meet. Abstr. MA2022-02 (2022), https://doi.org/10.1149/MA2022-02142475mtgabs, 2475–2475.
[32] J.V. de Sousa Araujo, M.X. Milagre, X. Zhou, I. Costa, An assessment of pitting corrosion in anodized aluminum alloys: it might not be what it seems, Mater. Corros. (2024), https://doi.org/10.1002/maco.202313977.
[33] Y. Ma, X. Chen, X. Zhou, Y. Yi, Y. Liao, W. Huang, Microstructural origin of localized corrosion in anodized AA2099-T8 aluminium–lithium alloy, Surf. Interface Anal. 48 (2016) 739–744, https://doi.org/10.1002/sia.5856.
[34] J.S. Pinheiro, H.R.P. Cardoso, K.R. Pereira, C. Radtke, S. Kunst, C.T. Oliveira, J. Z. Ferreira, Chromium/nickel-free conversion coating as cold post-treatment to anodized AA2024-T3 for corrosion resistance increase, Surf. Coat. Technol. 480 (2024) 130566, https://doi.org/10.1016/j.surfcoat.2024.130566.
[35] D.K. Heller, W.G. Fahrenholtz, M.J. O'Keefe, The effect of post-treatment time and temperature on cerium-based conversion coatings on Al 2024-T3, Corros. Sci. 52 (2010) 360–368, https://doi.org/10.1016/j.corsci.2009.09.023.
[36] H. Wu, Y. Ma, W. Huang, X. Zhou, K. Li, Y. Liao, Z. Wang, Z. Liang, L. Liu, Effect of iron-containing intermetallic particles on film structure and corrosion resistance of anodized AA2099 alloy, J. Electrochem. Soc. 165 (2018) C573–C581, https://doi.org/10.1149/2.1361809jes.
[37] Y. Ma, K. Li, X. Zhou, H. Wu, P. Zhu, B. Yang, Y. Liao, S. He, Effect of barrier layer on corrosion resistance of porous-type anodic films formed on AA2055 Al–Cu–Li alloy and pure aluminum, J. Electrochem. Soc. 167 (2020) 041508, https://doi.org/10.1149/1945-7111/ab75fe.
[38] K. Shimizu, G.M. Brown, H. Habazaki, K. Kobayashi, P. Skeldon, G.E. Thompson, G.C. Wood, Selective oxidation of aluminium and interfacial enrichment of iron during anodic oxide growth on an Al6Fe phase, Corros. Sci. 42 (2000) 831–840, https://doi.org/10.1016/S0010-938X(99)00108-0.
[39] L.E. Fratila-Apachitei, J. Duszczyk, L. Katgerman, Voltage transients and morphology of AlSi(Cu) anodic oxide layers formed in H_2SO_4 at low temperature, Surf. Coat. Technol. 157 (2002) 80–94, https://doi.org/10.1016/S0257-8972(02)00144-5.
[40] E. Zhuravlyova, L. Iglesias-Rubianes, A. Pakes, P. Skeldon, G.E. Thompson, X. Zhou, T. Quance, M.J. Graham, H. Habazaki, K. Shimizu, Oxygen evolution within barrier oxide films, Corros. Sci. 44 (2002) 2153–2159, https://doi.org/10.1016/S0010-938X(02)00025-2.
[41] S.-M. Moon, M. Sakairi, H. Takahashi, Application of CSLM to the surface morphological study of Al 5052 alloy anodized in sulfuric acid solution, J. Electrochem. Soc. 150 (2003) B473, https://doi.org/10.1149/1.1603248.
[42] L.E. Fratila-Apachitei, J. Duszczyk, L. Katgerman, AlSi(Cu) anodic oxide layers formed in H_2SO_4 at low temperature using different current waveforms, Surf. Coat. Technol. 165 (2003) 232–240, https://doi.org/10.1016/S0257-8972(02)00733-8.
[43] S.M. Moon, M. Sakairi, H. Takahashi, Behavior of second-phase particles in Al5052 alloy during anodizing in a sulfuric acid solution CSLM observation, J. Electrochem. Soc. 151 (2004) 399–405, https://doi.org/10.1149/1.1752933.
[44] L.E. Fratila-Apachitei, H. Terryn, P. Skeldon, G.E. Thompson, J. Duszczyk, L. Katgerman, Influence of substrate microstructure on the growth of anodic oxide layers, Electrochim. Acta 49 (2004) 1127–1140, https://doi.org/10.1016/j.electacta.2003.10.024.
[45] J.M. Runge, A.J. Pomis, Base metal microstructural considerations for aluminum finishing, AESF Sur/Fin (2004) 295–311.
[46] M. Curioni, M. Saenz De Miera, P. Skeldon, G.E. Thompson, J. Ferguson, Macroscopic and local filming behavior of AA2024-T3 aluminum alloy during anodizing in sulfuric acid electrolyte, J. Electrochem. Soc. 155 (2008) 387–395, https://doi.org/10.1149/1.2931522.
[47] M. Saenz de Miera, M. Curioni, P. Skeldon, G.E. Thompson, Modelling the anodizing behavior of aluminum alloys in sulfuric acid through alloy analogues, Corros. Sci. 50 (2008) 3410–3415, https://doi.org/10.1016/j.corsci.2008.09.019.
[48] J.-H. Liu, M. Li, S.-M. Li, M. Huang, Effect of the microstructure of Al 7050-T7451 on anodic oxide formation in sulfuric acid, Int. J. Miner. Metall. Mater. 16 (2009) 432–438, https://doi.org/10.1016/S1674-4799(09)60076-5.
[49] H. Zhu, X. Zhang, M.J. Couper, A.K. Dahle, Effect of initial microstructure on surface appearance of anodized aluminum extrusions, Metall. Mater. Trans. A 40 (2009) 3264–3275, https://doi.org/10.1007/s11661-009-9976-0.
[50] M. Saenz De Miera, M. Curioni, P. Skeldon, G.E. Thompson, Preferential anodic oxidation of second-phase constituents during anodizing of AA2024-T3 and AA7075-T6 alloys, Surf. Interface Anal. 42 (2010) 241–246, https://doi.org/10.1002/sia.3191.
[51] M. Saenz de Miera, M. Curioni, P. Skeldon, G.E. Thompson, The behavior of second-phase particles during anodizing of aluminum alloys, Corros. Sci. 52 (2010) 2489–2497, https://doi.org/10.1016/j.corsci.2010.03.029.
[52] F. Viejo, A.E. Coy, F.J. García-García, M.C. Merino, Z. Liu, P. Skeldon, G. E. Thompson, Enhanced performance of the AA2050-T8 aluminum alloy following excimer laser surface melting and anodizing processes, Thin Solid Films 518 (2010) 2722–2731, https://doi.org/10.1016/j.tsf.2009.09.121.
[53] M. Jariyaboon, P. Møller, R.E. Dunin-Borkowski, R. Ambat, FIB-SEM investigation of trapped intermetallic particles in anodic oxide films on AA1050 aluminum, Anti-Corros. Methods Mater. 58 (2011) 173–178, https://doi.org/10.1108/00035591111148885.
[54] M. Mokaddem, J. Tardelli, K. Ogle, E. Rocca, P. Volovitch, Atomic emission spectroelectrochemical investigation of the anodization of AA7050T74 aluminum alloy, Electrochem. Commun. 13 (2011) 42–45, https://doi.org/10.1016/j.elecom.2010.11.008.
[55] S. Moon, Y. Nam, C. Yang, Y. Jeong, Growth of anodic oxide films on AC2A alloy in sulphuric acid solution, Corros. Sci. 53 (2011) 1547–1553, https://doi.org/10.1016/j.corsci.2011.01.029.
[56] A. Forn, M.T. Baile, J.A. Picas, E. Martín, S. Menargues, Anodizing effect on the wear and corrosion behavior of en AC-46500 components produced by semi-solid rheocasting (SSR), AIP Conf. Proc. 1353 (2011) 1069–1074, https://doi.org/10.1063/1.3589658.
[57] Y. Ma, X. Zhou, G.E. Thompson, M. Curioni, T. Hashimoto, P. Skeldon, P. Thomson, M. Fowles, Anodic film formation on AA2099-T8 aluminum alloy in tartaric–sulfuric acid, J. Electrochem. Soc. 158 (2011) C17–C22, https://doi.org/10.1149/1.3523262.
[58] A.B.C. Fares, M.A. Belouchrani, S. Bellayer, T. Boukharouba, Influence of intermetallic compounds and metallurgical state of the 2017A aluminium alloy on the morphology of alumina films developed by anodic oxidation, J. Tribol. Surf. Eng. 2 (2011) 239–251.
[59] J. Tardelli, E. Rocca, Electrochemical behaviour of intermetallic phases in sulfuric acid at high voltage—anodization of Al7Cu2Fe and MgZn2 phase, Corros. Sci. (2011).
[60] F. Riddar, S. Hogmark, Å.K. Rudolphi, Comparison of anodized aluminum surfaces from four fabrication methods, J. Mater. Process. Technol. 212 (2012) 2272–2281, https://doi.org/10.1016/j.jmatprotec.2012.06.007.
[61] J.M. Runge, Trace elements and their impact on surface finishing characteristics of aluminum extrusions, in: *Proc. ET*, Miami, 2012.
[62] L. Chauke, H. Möller, U.A. Curle, G. Govender, Anodising of Al-Mg-Si-(Cu) alloys produced by R-HPDC, Mater. Sci. Forum 765 (2013) 658–662, https://doi.org/10.4028/www.scientific.net/MSF.765.658.
[63] Y.S. Huang, T.S. Shih, J.H. Chou, Electrochemical behavior of anodized AA7075-T73 alloys as affected by the matrix structure, Appl. Surf. Sci. 283 (2013) 249–257, https://doi.org/10.1016/j.apsusc.2013.06.094.
[64] C. Fares, A. Boudiaf, M.E.A. Belouchrani, T. Boukharouba, Microstructural characterisation of oxide layer developed by sulphuric anodisation on 2017A alloys, Int. J. Mater. Res. 104 (2013) 1108–1113, https://doi.org/10.3139/146.110962.
[65] F. Bertram, F. Zhang, J. Evertsson, F. Carlà, J. Pan, M.E. Messing, A. Mikkelsen, J. O. Nilsson, E. Lundgren, In situ anodization of aluminum surfaces studied by x-ray reflectivity and electrochemical impedance spectroscopy, J. Appl. Phys. 116 (2014), https://doi.org/10.1063/1.4890318.
[66] C. Levy, M. Kalenda, G. Gonasagren, Corrosion behaviour of the anodised A356 aluminium alloy produced by the rheo-high pressure die casting process, Adv. Mater. Res. 1019 (2014) 67–73, https://doi.org/10.4028/www.scientific.net/AMR.1019.67.
[67] J.C. Miramontes, C. Gaona Tiburcio, E. García Mata, M.Á. Esneider Alcála, E. Maldonado-Bandala, M. Lara-Banda, D. Nieves-Mendoza, J. Olguín-Coca, P. Zambrano-Robledo, L.D. López-León, Corrosion resistance of aluminum alloy AA2024 with hard anodizing in sulfuric acid-free solution, Materials 15 (2022) 6401, https://doi.org/10.3390/ma15186401.
[68] O. Jilani, N. Njah, P. Ponthiaux, Corrosion properties of anodized aluminum: effects of equal channel angular pressing prior to anodization, Corros. Sci. 89 (2014) 163–170, https://doi.org/10.1016/j.corsci.2014.08.020.
[69] Y. Zhu, S. Wang, Q. Yang, F. Zhou, Effect of Fe- and Si-enriched secondary precipitates and surface roughness on pore formation on aluminum plate surfaces during anodizing, J. Mater. Eng. Perform. 23 (2014) 3389–3399, https://doi.org/10.1007/s11665-014-1116-3.

[70] S.-M. Li, Y.-D. Li, Y. Zhang, J.-H. Liu, M. Yu, Effect of intermetallic phases on the anodic oxidation and corrosion of 5A06 aluminum alloy, Int. J. Miner. Metall. Mater. 22 (2015) 167–174, https://doi.org/10.1007/s12613-015-1057-3.

[71] B. Zhu, P. Leisner, S. Seifeddine, A.E.W. Jarfors, Influence of Si and cooling rate on microstructure and mechanical properties of Al-Si-Mg cast alloys, Surf. Interface Anal. 48 (2015) 861–869, https://doi.org/10.1002/sia.5814.

[72] J.M. Runge, T. Hossain, Interfacial phenomena in 7000 series alloys and their impact on the anodic oxide, Mater. Today.: Proc. 2 (2015) 3753–3761, https://doi.org/10.1016/j.matpr.2015.10.096.

[73] J.M. Runge, Anodizing complex 7000 series, Light Met. Age 74 (2016) 52–56.

[74] F. Zhang, J. Nilsson, J. Pan, In situ and operando AFM and EIS studies of anodization of Al 6060: influence of intermetallic particles, J. Electrochem. Soc. 163 (2016) C609–C618, https://doi.org/10.1149/2.0061610jes.

[75] D. Nickel, D. Dietrich, R. Morgenstern, I. Scharf, H. Podlesak, T. Lampke, Anodisation of aluminium alloys by micro-capillary technique as a tool for reliable, cost-efficient, and quick process parameter determination, Adv. Mater. Sci. Eng. 2016 (2016) 1–12, https://doi.org/10.1155/2016/1374897.

[76] D. Veys-Renaux, N. Chahboun, E. Rocca, Anodizing of multiphase aluminium alloys in sulfuric acid: in-situ electrochemical behaviour and oxide properties, Electrochim. Acta 211 (2016) 1056–1065, https://doi.org/10.1016/j.electacta.2016.06.131.

[77] B. Zhu, S. Seifeddine, P.O.Å. Persson, A.E.W. Jarfors, P. Leisner, C. Zanella, A study of formation and growth of the anodised surface layer on cast Al-Si alloys based on different analytical techniques, Mater. Des. 101 (2016) 254–262, https://doi.org/10.1016/j.matdes.2016.04.013.

[78] D. Caliari, G. Timelli, T. Salata, G. Cavagnini, S. Maestri, Surface defects of anodized HPDC Al alloy components, Metall. Ital. 108 (2016) 69–72.

[79] Y.D. Li, P.Z. Zhao, S.M. Li, Optimization for anodizing conditions of 5A06 aluminum alloy based on doehlert design matrix method, Mater. Sci. Forum 877 (2017) 498–507, https://doi.org/10.4028/www.scientific.net/MSF.877.498.

[80] J.M. Runge, Base metal microstructural considerations for anodizing aluminum extrusions, in: *Proc. Eleventh Int. Aluminum Extrusion Technol. Seminar*, Chicago, 2016.

[81] J.M. Runge, Understanding the interface: Meeting the challenges of anodizing cast substrates, in: *Proc. 2016 AAC Annu. Tech. Conf. Exposition*, Montreal, Canada, 2016.

[82] L. Hu, D. Chen, F. Shi, S. Chen, Effect of AlSiFe on the anodizing process of 6063 aluminum, Surf. Interface Anal. 48 (2016) 1299–1304, https://doi.org/10.1002/sia.6036.

[83] B. Zhu, M. Fedel, N.-E. Andersson, P. Leisner, F. Deflorian, C. Zanella, Effect of Si content and morphology on corrosion resistance of anodized cast Al-Si alloys, J. Electrochem. Soc. 164 (2017) C435–C441, https://doi.org/10.1149/2.1631707jes.

[84] P. Atz Dick, G.H. Knörnschild, L.F.P. Dick, Anodising and corrosion resistance of AA 7050 friction stir welds, Corros. Sci. 114 (2017) 28–36, https://doi.org/10.1016/j.corsci.2016.10.015.

[85] M. Bononi, M. Conte, R. Giovanardi, A. Bozza, Hard anodizing of AA2099-T8 aluminum lithium copper alloy: influence of electric cycle, electrolytic bath composition and temperature, Surf. Coat. Technol. 325 (2017) 627–635, https://doi.org/10.1016/j.surfcoat.2017.07.028.

[86] M.A. Arenas, A. Conde, J.J. De Damborenea, Effect of acid traces on hydrothermal sealing of anodising layers on 2024 aluminium alloy, Electrochim. Acta 55 (2010) 8704–8708, https://doi.org/10.1016/j.electacta.2010.07.057.

[87] J. Liu, G. Rong, S. Cen, S. Li, H. Shi, K. Zhao, M. Yu, Dissolution behavior of intermetallic particles in AA2297-T87 during anodizing in adipic-sulfuric acid, J. Electrochem. Soc. 165 (2018) C980–C990, https://doi.org/10.1149/2.0061816jes.

[88] M. Bononi, R. Giovanardi, Hard anodizing of AA2011-T3 Al-Cu-Pb-Bi free-cutting alloy: Improvement of the process parameters, Corros. Sci. 141 (2018) 63–71, https://doi.org/10.1016/j.corsci.2018.07.004.

[89] S.A. Abdel-Gawad, W.M. Osman, A.M. Fekry, Characterization and corrosion behavior of anodized aluminum alloys for military industries applications in artificial seawater, Surf. Interfaces 14 (2019) 314–323, https://doi.org/10.1016/j.surfin.2018.08.001.

[90] B. Díaz, R. Figueroa, X.R. Nóvoa, C. Pérez, S. Pérez-Betanzos, S. Valverde-Pérez, Effect of substrate microstructure on corrosion resistance of cast and forged anodised 6082 Al alloy, Surf. Coat. Technol. 481 (2024) 130614, https://doi.org/10.1016/j.surfcoat.2024.130614.

[91] E. Razzouk, D. Koncz-Horváth, T.I. Török, Microstructure effects on anodizing high-silicon aluminium alloy AlSi12Cu1(Fe) under various surface conditions and power modes, Crystals 14 (2024) 352, https://doi.org/10.3390/cryst14040352.

[92] H.A. Elkilany, M.A. Shoeib, O.E. Abdel-Salam, Influence of hard anodizing on the mechanical and corrosion properties of different aluminum alloys, Metallogr. Microstruct. Anal. 8 (2019) 861–870, https://doi.org/10.1007/s13632-019-00594-5.

[93] B. Zhu, S. Seifeddine, A.E.W. Jarfors, P. Leisner, C. Zanella, A study of anodising behaviour of Al-Si components produced by rheocasting, Solid State Phenom. 285 (2019) 39–44, https://doi.org/10.4028/www.scientific.net/SSP.285.39.

[94] H. Shi, M. Yu, J. Liu, G. Rong, R. Du, J. Wang, S. Li, Effect of alkaline etching on microstructure and anticorrosion performance of anodic film on Al-Mg-Si alloy, Corros. Sci. 169 (2020) 108642, https://doi.org/10.1016/j.corsci.2020.108642.

[95] F. Zhang, C. Örnek, J.O. Nilsson, J. Pan, Anodisation of aluminium alloy AA7075 – Influence of intermetallic particles on anodic oxide growth, Corros. Sci. 164 (2020) 108319, https://doi.org/10.1016/j.corsci.2019.108319.

[96] S.U. Okene, M. Abdullahi, A. Gana, Corrosion improvement of AA7075 through precipitation hardness and anodization, Mater. Today.: Proc. 38 (2021) 729–736, https://doi.org/10.1016/j.matpr.2020.04.084.

[97] N.N. Regone, C.M.A. Freire, M. Ballester, Al-based anodic oxide films structure observation using field emission gun scanning electron microscopy, J. Mater. Process. Technol. 172 (2006) 146–151, https://doi.org/10.1016/j.jmatprotec.2005.09.005.

[98] U. Malayoglu, K.C. Tekin, U. Malayoglu, S. Shrestha, An investigation into the mechanical and tribological properties of plasma electrolytic oxidation and hard-anodized coatings on 6082 aluminum alloy, Mater. Sci. Eng. A 528 (2011) 7451–7460, https://doi.org/10.1016/j.msea.2011.06.032.

[99] L. Vojkuvka, A. Santos, J. Pallarès, J. Ferré-Borrull, L.F. Marsal, J.P. Celis, On the mechanical properties of nanoporous anodized alumina by nanoindentation and sliding tests, Surf. Coat. Technol. 206 (2012) 2115–2124, https://doi.org/10.1016/j.surfcoat.2011.09.040.

[100] L. Winter, T. Lampke, Fatigue resistance of an anodized and hardanodized 6082 aluminum alloy depending on the coating thickness in the high cycle regime, Adv. Eng. Mater. 25 (2023) 2300394, https://doi.org/10.1002/adem.202300394.

[101] N.N. Regone, C.M.A. Freire, M. Ballester, N.A. Mariano, E.N. Codaro, H.A. Acciari, Analysis of the mechanical properties of anodized Al-Si alloys, Mater. Res. 25 (2022), https://doi.org/10.1590/1980-5373-mr-2022-0044.

[102] E. Dervishi, M. McBride, R. Edwards, M. Gutierrez, N. Li, R. Buntyn, D.E. Hooks, Mechanical and tribological properties of anodic Al coatings as a function of anodizing conditions, Surf. Coat. Technol. 444 (2022) 128652, https://doi.org/10.1016/j.surfcoat.2022.128652.

[103] M. Hou, C. Pan, M. Wang, D.-H. Xia, Z. Qin, W. Hu, Improving the cavitation corrosion resistance of 6061 aluminum alloy by anodizing, Electrochim. Acta 503 (2024) 144890, https://doi.org/10.1016/j.electacta.2024.144890.

[104] B.J. Usman, F. Scenini, M. Curioni, Exploring the use of an AC-DC-AC technique for the accelerated evaluation of anticorrosion performance of anodic films on aluminium alloys, Prog. Org. Coat. 144 (2020) 105648, https://doi.org/10.1016/j.porgcoat.2020.105648.

[105] B.J. Usman, F. Scenini, M. Curioni, Corrosion testing of anodized aerospace alloys: comparison between immersion and salt spray testing using electrochemical impedance spectroscopy, J. Electrochem. Soc. 167 (2020) 041505, https://doi.org/10.1149/1945-7111/AB74E3.

[106] B.J. Usman, M. Curioni, Influence of temperature on the corrosion testing of anodized aerospace alloys, Corros. Sci. 192 (2021) 109772, https://doi.org/10.1016/j.corsci.2021.109772.

[107] B.J. Usman, F. Scenini, M. Curioni, The effect of exposure conditions on performance evaluation of post-treated anodic oxides on an aerospace aluminium alloy: comparison between salt spray and immersion testing, Surf. Coat. Technol. 399 (2020) 126157, https://doi.org/10.1016/j.surfcoat.2020.126157.

[108] J. Qin, M. Curioni, Transitions in porous oxide morphologies on AA2024-T3 anodized under high currents and low temperatures: impact on corrosion behaviour, Electrochim. Acta 428 (2022) 140927, https://doi.org/10.1016/j.electacta.2022.140927.

[109] X. Chen, Z. Liu, W. Liu, Effects of tartaric acid on the structure and corrosion resistance for anodizing films of aerospace aluminium alloys, Mater. Res. Innov. 28 (2024) 1–7, https://doi.org/10.1080/14328917.2023.2212486.

[110] J.R. Davis, Aluminium and Aluminium Alloys, ASM International, Materials Park, 1993.

[111] E. Kock, C.Dr. Gerlach, M.Dr. Beneke, Anodizing process for aluminum materials, *Patent* DE10361888B3, 2004.

[112] T.J. Collins, ImageJ for microscopy, Biotechniques 43 (2007), https://doi.org/10.2144/000112517.

[113] J.V. de Sousa Araujo, I. Costa, X. Zhou, Comparison of constituent intermetallic particles in different aluminium alloys, Metallogr. Microstruct. Anal. (2025), https://doi.org/10.1007/s13632-025-01170-w.

[114] Y. Ma, X. Zhou, G.E. Thompson, T. Hashimoto, P. Thomson, M. Fowles, Distribution of intermetallics in an AA2099-T8 aluminium alloy extrusion, Mater. Chem. Phys. 126 (2011) 46–53, https://doi.org/10.1016/j.matchemphys.2010.12.014.

[115] I.S. Molchan, T.V. Molchan, N.V. Gaponenko, P. Skeldon, G.E. Thompson, Impurity-driven defect generation in porous anodic alumina, Electrochem. Commun. 12 (2010) 693–696, https://doi.org/10.1016/j.elecom.2010.03.002.

[116] H. Takahashi, M. Chiba, Role of anodic oxide films in the corrosion of aluminum and its alloys, Corros. Rev. 36 (2018) 35–54, https://doi.org/10.1515/corrrev-2017-0048.

[117] Y. Ma, X. Zhou, G.E. Thompson, M. Curioni, X. Zhong, E. Koroleva, P. Skeldon, P. Thomson, M. Fowles, Discontinuities in the porous anodic film formed on AA2099-T8 aluminium alloy, Corros. Sci. 53 (2011) 4141–4151, https://doi.org/10.1016/j.corsci.2011.08.023.

[118] C.M. MacRae, A.E. Hughes, J.S. Laird, A.M. Glenn, N.C. Wilson, A. Torpy, M. A. Gibson, X. Zhou, N. Birbilis, G.E. Thompson, An examination of the composition and microstructure of coarse intermetallic particles in AA2099-T8, including Li detection, Microsc. Microanal. 24 (2018) 1–17, https://doi.org/10.1017/S1431927618000454.

[119] K. Tzoganakou, P. Skeldon, G.E. Thompson, X. Zhou, U. Kreissig, E. Wieser, H. Habazaki, K. Shimizu, Mobility of lithium ions in anodic alumina formed on an Al-Li alloy, Corros. Sci. 42 (2000) 1083–1091, https://doi.org/10.1016/S0010-938X(99)00130-4.

[120] Y. Ma, X. Zhou, G.E. Thompson, X. Zhang, C. Luo, M. Curioni, H. Liu, Microstructural modification arising from alkaline etching and its effect on anodizing behavior of Al-Li-Cu alloy extrusion direction, J. Electrochem. Soc. 160 (2013) C111, https://doi.org/10.1149/2.043303jes.

[121] J. Huang, S. Feng, S. Li, C. Wu, J. Chen, The crystallographic corrosion and its microstructure in an Al-Cu-Li alloy, J. Alloy. Compd. 861 (2021) 158588, https://doi.org/10.1016/j.jallcom.2020.158588.
[122] X. Zhang, X. Zhou, T. Hashimoto, B. Liu, Localized corrosion in AA2024-T351 aluminium alloy: transition from intergranular corrosion to crystallographic pitting, Mater. Charact. 130 (2017) 230–236, https://doi.org/10.1016/j.matchar.2017.06.022.
[123] M.O.A. Ferreira, J.P.L. Nascimento, N.B. Leite, A. de Siervo, G.L. Fernandes, A. R. Vaz, R.V. Gelamo, I.V. Aoki, J.A. Moreto, The potentialities of Raman and XPS techniques to evaluate the corrosion products formed on the 2198-T851 aluminium alloy exposed to sodium chloride solution, Mater. Res. 26 (2023), https://doi.org/10.1590/1980-5373-mr-2022-0453.
[124] A. Ul-Hamid, A Beginner's Guide to Scanning Electron Microscopy, Springer International Publishing, Cham, 2018, https://doi.org/10.1007/978-3-319-98482-7.
[125] M.B. Jensen, A. Guerard, D.E. Tallman, G.P. Bierwagen, Studies of electron transfer at aluminum alloy surfaces by scanning electrochemical microscopy, J. Electrochem. Soc. 155 (2008) C324, https://doi.org/10.1149/1.2916734.
[126] T.J. Shaffner, R.D. Van Veld, "Charging" effects in the scanning electron microscope, J. Phys. E 4 (1971) 633–637, https://doi.org/10.1088/0022-3735/4/9/002.
[127] M.A. Páez, T.M. Foong, C.T. Ni, G.E. Thompson, K. Shimizu, H. Habazaki, P. Skeldon, G.C. Wood, Barrier-type anodic film formation on an Al-3.5 wt% Cu alloy, Corros. Sci. 38 (1996) 59–72, https://doi.org/10.1016/0010-938X(96)00102-3.
[128] H. Habazaki, K. Shimizu, P. Skeldon, G.E. Thompson, G.C. Wood, The incorporation of metal ions into anodic films on aluminium alloys, Philos. Mag. B 73 (1996) 445–460, https://doi.org/10.1080/13642819608239128.
[129] H. Habazaki, K. Shimizu, P. Skeldon, G.E. Thompson, G.C. Wood, The co-enrichment of alloying elements in the substrate by anodic oxidation of Al-Cu-W alloys, Corros. Sci. 39 (1997) 339–354, https://doi.org/10.1016/S0010-938X(97)83350-1.
[130] H. Habazaki, K. Shimizu, M.A. Paez, P. Skeldon, G.E. Thompson, G.C. Wood, X. Zhou, Oxidation of copper and mobility of copper ions during anodizing of an Al–1.5 wt% Cu alloy, Surf. Interface Anal. 23 (1995) 892–898, https://doi.org/10.1002/sia.740231307.
[131] J.M. Torrescano-Alvarez, M. Curioni, P. Skeldon, Gravimetric measurement of oxygen evolution during anodizing of aluminum alloys, J. Electrochem. Soc. 164 (2017) C728–C733, https://doi.org/10.1149/2.0371713jes.
[132] Y. Sepulveda, M.A. Paez, J.H. Zagal, J. Henriquez, J. Pavez, A. Monsalve, O. Bustos, G.E. Thompson, Anodizing of Al 2024-T3 in mixtures of sulphuric-boric acids, Bol. Soc. Chil. Quím. 46 (2001) 399–407, https://doi.org/10.4067/S0366-16442001000400003.
[133] P. Skeldon, G.E. Thompson, G.C. Wood, X. Zhou, H. Habazaki, K. Shimizu, Evidence of oxygen bubbles formed within anodic films on aluminium-copper alloys, Philos. Mag. A 75 (1997) 729–741, https://doi.org/10.1080/01418619708214206.
[134] J. Cabral-Miramontes, N. Cabral-Miramontes, D. Nieves-Mendoza, M. Lara-Banda, E. Maldonado-Bandala, J. Olguín-Coca, L.D. Lopez-Leon, F. Estupiñan-Lopez, F. A. Calderon, C. Gaona Tiburcio, Anodizing of AA2024 aluminum–copper alloy in citric-sulfuric acid solution: effect of current density on corrosion resistance, Coatings 14 (2024) 816, https://doi.org/10.3390/coatings14070816.
[135] C.E. Caicedo-Martinez, G.E. Thompson, E.V. Koroleva, Nanoscale engineering of aluminium surfaces, Surf. Eng. 18 (2002) 145–150, https://doi.org/10.1179/026708401225002712.
[136] C.E. Caicedo-Martinez, E. Koroleva, P. Skeldon, G.E. Thompson, G. Hoellrigl, P. Bailey, T.C.Q. Noakes, H. Habazaki, K. Shimizu, Behavior of impurity and minor alloying elements during surface treatments of aluminum, J. Electrochem. Soc. 149 (2002) B139, https://doi.org/10.1149/1.1457982.
[137] J.V. de Sousa Araujo, A. de, F. Santos Bugarin, U. Donatus, C. de, S.C. Machado, F. M. Queiroz, M. Terada, A. Astarita, I. Costa, Thermomechanical treatment and corrosion resistance correlation in the AA2198 Al–Cu–Li alloy, Corros. Eng. Sci. Technol. 54 (2019) 575–586, https://doi.org/10.1080/1478422X.2019.1637077.
[138] J.A. Moreto, C.E.B. Marino, W.W. Bose Filho, L.A. Rocha, J.C.S. Fernandes, SVET, SKP and EIS study of the corrosion behaviour of high strength Al and Al–Li alloys used in aircraft fabrication, Corros. Sci. 84 (2014) 30–41, https://doi.org/10.1016/j.corsci.2014.03.002.
[139] Y. Lv, T. Hashimoto, X. Zhou, X. Zhang, Influence of thermomechanical treatment on the corrosion behaviour of 2A97 Al-Cu-Li alloy, Corros. Commun. 15 (2024) 13–23, https://doi.org/10.1016/j.corcom.2023.10.003.
[140] Y.-L. Ma, X.-R. Zhou, X.-M. Meng, W.-J. Huang, Y. Liao, X.-L. Chen, Y.-N. Yi, X.-X. Zhang, G.E. Thompson, Influence of thermomechanical treatments on localized corrosion susceptibility and propagation mechanism of AA2099 Al–Li alloy, Trans. Nonferrous Met. Soc. China 26 (2016) 1472–1481, https://doi.org/10.1016/S1003-6326(16)64252-8.
[141] Y. Chen, F. Kong, J. Yang, X. Song, X. Meng, Damage behavior of 2198-T8 Al-Li alloy with different corrosion fatigue modes, Int. J. Fatigue 156 (2022) 106671, https://doi.org/10.1016/j.ijfatigue.2021.106671.
[142] C. Charalampidou, W. Dietzel, M. Zheludkevich, S.K. Kourkoulis, N. D. Alexopoulos, Corrosion-induced mechanical properties degradation of Al-Cu-Li (2198-T351) aluminium alloy and the role of side-surface cracks, Corros. Sci. 183 (2021) 109330, https://doi.org/10.1016/j.corsci.2021.109330.
[143] N.D. Alexopoulos, A. Proiou, T. Examilioti, N. Kashaev, S. Riekehr, S. K. Kourkoulis, Effect of artificial aging on the mechanical performance of (Al-Cu) 2024 and (Al-Cu-Li) 2198 aluminum alloys, Procedia Struct. Integr. 2 (2016) 3782–3783, https://doi.org/10.1016/j.prostr.2016.06.470.
[144] M. Lerner, Is the barrier layer responsible for the cellular structure of aluminum oxide film anodized in sulfuric acid?, in: *Proc. AESF Surfin Conf.*, Chicago, 2003.
[145] J. Araujo, R. Pereira, R. Klumpp, I. Costa, O processo de anodização do alumínio e suas ligas: uma abordagem histórica e eletroquímica, Quím. Nova (2021), https://doi.org/10.21577/0100-4042.20170748.
[146] H.M. Obispo, L.E. Murr, R.M. Arrowood, E.A. Trillo, Copper deposition during the corrosion of aluminum alloy 2024 in sodium chloride solutions, Corros. Sci. (2000).
[147] G.C. Wood, J.P. O'Sullivan, The anodizing of aluminium in sulphate solutions, Electrochim. Acta 15 (1970) 1865–1876, https://doi.org/10.1016/0013-4686(70)85024-1.
[148] U. Donatus, M.O. Bodunrin, A. Olayinka, M.X. Milagre, O.R. Oloyede, S. Aribo, J. V. de Sousa Araujo, C. de, S.C. Machado, I. Costa, Corrosion resistance of precipitation-hardened Al alloys: a comparison between new generation Al-Cu-Li and conventional alloys. Adv. Aluminium Compos. Alloys, IntechOpen, 2021, https://doi.org/10.5772/intechopen.92807.
[149] G. Svenningsen, M.H. Larsen, J.H. Nordlien, K. Nisancioglu, Effect of thermomechanical history on intergranular corrosion of extruded AlMgSi(Cu) model alloy, Corros. Sci. 48 (2006) 3969–3987, https://doi.org/10.1016/j.corsci.2006.03.018.
[150] T. Hashimoto, G.E. Thompson, X. Zhou, P.J. Withers, 3D imaging by serial block face scanning electron microscopy for materials science using ultramicrotomy, Ultramicroscopy 163 (2016) 6–18, https://doi.org/10.1016/j.ultramic.2016.01.005.
[151] E. Schmidl, R. Pippig, R. Morgenstern, T. Lampke, I. Scharf, Nondestructive analysis of pitting corrosion characteristics on EN AW-2024-T3 using 3D optical pattern profilometry, Corros. Eng. Sci. Technol. 53 (2018) 194–198, https://doi.org/10.1080/1478422X.2018.1427845.
[152] M. Li, A. Seyeux, F. Wiame, P. Marcus, J. Światowska, Localized corrosion induced surface modifications of Al-Cu-Li alloy studied by ToF-SIMS 3D imaging, npj Mater. Degrad. 5 (2021) 23, https://doi.org/10.1038/s41529-021-00170-9.
[153] T. Hashimoto, X. Zhang, X. Zhou, P. Skeldon, S.J. Haigh, G.E. Thompson, Investigation of dealloying of S phase (Al_2CuMg) in AA 2024-T3 aluminium alloy using high resolution 2D and 3D electron imaging, Corros. Sci. 103 (2016) 157–164, https://doi.org/10.1016/j.corsci.2015.11.013.